UNIVERSITEIT VAN PRETORIA
UNIVERSITY OF PRETORIA
YUNIBESITHI YA PRETORIA

Two-dimensional semiconductor transition metal dichalcogenide nanosheets as charge carriers in metallophthalocyanine based solar cells

By

Lebogang Manamela

(17226199)

Submitted in fulfilment of the requirements for the degree

Master of Science in Chemistry

In the Faculty of Natural & Agricultural Sciences

University of Pretoria

January 2020

© University of Pretoria

Declaration

I, Lebogang Manamela (17226199), declare that the dissertation, which I hereby submit for the degree Master of Sciences in chemistry, at the University of Pretoria, is my own work and has not previously been submitted by me for a degree at this or any other tertiary institution.

Signature: …………………

Date: ……………………….

© University of Pretoria

Dedication

This work is dedicated to my mother, Nkwe Onicia Manamela and my Manamela family, My father Mologadi Ludwick Mabotja and my Mabotja family, my son Amogelang Moshia and my girlfriend Kedibone Mmasago Moshia.

© University of Pretoria

Acknowledgements

I would like to acknowledge the following people and departments:

- I would like to thank God Almighty for giving me power and strength to embark on this academic journey.
- I would like to express my gratitude to my supervisors, Dr N Nombona and Prof M. Diale for their guidance and support throughout this study.
- I would like to acknowledge my parents and families for their support throughout this journey, both emotionally and financially.
- My gratitude goes to my mentor Mr Juvet Fru for his constant guidance and always being available when I need help.
- I would like to thank my colleagues from Nombona group from their moral and emotional support.
- I would like to thank my colleagues from the Clean and Green Energy group for their support.
- I would like to express my gratitude to Dr Mlambo for assistance with Raman characterisation
- I would like to acknowledge the Laboratory for Microscopy and Microanalysis for allowing me to use their instruments for SEM and EDX analysis.
- I would like to thank the University of Pretoria, Faculty of Natural and Agricultural Sciences, Department of Chemistry and Physics for giving me the environment for pursuing Masters in Chemistry.
- I would like to thank NRF for giving me financial support.

© University of Pretoria

Abstract

Two-dimensional (2D) materials have received widespread attention as prime candidates for scientific research in the fields of optoelectronics and photonic applications. This thesis focuses on the use of transition metal dichalcogendes (TMDs) for solar cell application.

TMDs are compounds with the general formula MX_2, where M is transition metal and X is chalcogen and most of them are intrinsically n-type. These materials are arranged as layers stacked together by weak van der Waals forces. They have found application in solar cells due to their high carrier mobility, chemical stability and flexibility. Exfoliation of the bulk TMDs maintains these properties and further imparts more properties such as switching the bandgap from indirect to direct and this further increases the carrier mobility of the material.

In this work we explore the use of molybdenum sulfide (MoS_2) and tungsten (WS_2) TMDs as electron transporting layers for solar cell application. The TMDs were successfully synthesised using the chemical exfoliation method and they were further doped with gold (Au) in order to enhance charge carrier mobility. The doped and undoped TMDs were characterised using X-ray diffraction (XRD), Raman spectroscopy, energy-dispersive X-ray spectroscopy (EDS) and scanning electron microscopy (SEM).

These TMDs were used together with metallophthalocyanines (MPc's) as photon absorbers. MPc's are known to be thermally and chemically stable in addition to having a relatively high extinction coefficient in the visible range. In our study we show the photovoltaic properties of TMDs combined with a variety of MPc's. The utilisation of these TMDs with MPc's has led to the generation of cost-effective solar cells that can be exploited for future technological applications.

© University of Pretoria

UNIVERSITEIT VAN PRETORIA
UNIVERSITY OF PRETORIA
YUNIBESITHI YA PRETORIA

Contents

© University of Pretoria

© University of Pretoria

List of abbreviations

AC	Alternating current
ALD	Atomic layer deposition
C_{60}	(C60-Ih)[5,6]fullerene
CdTe	Cadmium telluride
CIGS	Copper indium gallium selenide
CuPc	Copper phthalocyanine
CVD	Chemical vapour deposition
DC	Direct current
DMF	Dimethylformamide
EDS	Energy-dispersive X-ray spectroscopy
ETL	Electron transporting layer
FePc	Iron phthalocyanine
FTO	Flourine doped tin oxide
HOMO	Highest occupied molecular orbital
HTL	Hole transporting layer
I-V	Current- Voltage
LUMO	Lowest unoccupied molecular orbital
MnPc	Manganese phthalocyanine
MPc	Metallophthalocyanine
NiPc	Nickel phthalocyanine
NMP	N-Methyl-2-pyrrolidone
PCBM	Phenyl-C61-butyric acid methyl ester
P3HT	Poly(3-hexylthiophene-2,5-diyl)
SEM	Scanning electron microscopy
TMD	Transition metal dichalcogenide
UV-vis	Ultraviolet- visible
XRD	X-ray diffraction

© University of Pretoria

List of Figures

© University of Pretoria

© University of Pretoria

© University of Pretoria

© University of Pretoria

List of Tables

© University of Pretoria

Chapter 1: Introduction

1.1 Background

Climate change and global warming occur mainly due to the release of CO_2 and other greenhouse gases into the atmosphere [1]. These greenhouse gases trap heat on the earth's surface and atmosphere resulting in an increase in the average temperature of the globe. The release of these harmful gases is mainly due to the burning of fossil fuels for energy generation. This suggests the need for the implementation of better technologies to mitigate this issue of climate change [2-3].

To lessen this problem, different types of solar cells have been employed. Strategical categorisation of these solar cells into different generations has seen researchers making progress in using them as fossil fuel substitutes [4]. Unfortunately, solar cells currently cannot completely supersede coal as a source of energy as challenges such as high cost of production (for the most efficient solar cells), stability and performance are still major limitations [4-5]. In this project, an attempt in addressing these challenges will be made by fabricating a solar cell with improved stability and it is hoped that the materials used will improve performance.

Solar cells are devices that have been developed to capture photons from the sun in order to produce electricity [5-6]. The major advantage of using solar cells is that they are small devices that can be used anywhere unlike current electrical technologies. Adding on to their advantages, the cost of the solar cell can be reduced by making use of cheap materials and they only require the abundant and free solar energy as a source [7-8]. A typical solar cell consists of an active layer, an electron transporting layer (ETL) (most often an n-type semiconductor), and a hole transporting layer (HTL) (most often a p-type semiconductor) sandwiched between two electrodes [9]. The active layer absorbs photons from the sunlight and generate an electron-hole pair. The electron transporting layer acts as a semipermeable membrane which only extracts and separates the electrons from the holes [9]. The electron is then taken to the cathode through an external circuit generating electricity, and finally gets to the anode where it recombines with the hole. The hole would, at the same time, have been extracted by the hole transporting layer, separated from the electron, and ultimately taken to the anode for recombination with the electron that has completed the circuit [10–12]. An efficient solar cell is designed such that the time the charges take to reach

© University of Pretoria

their respective membranes (p and n-type semiconductors) is smaller than the lifetime of the electron-hole pair [13-14]. However, the abovementioned mechanism doesn't occur as smoothly. Some solar cells experience frequent electron-hole recombination as their semiconducting materials have low carrier charge mobility. Some solar cells have materials that have low thermal and chemical stability resulting in a reduced lifetime of the solar cell [15].

There are three generations of solar cells [16–18]. The first-generation solar cells are currently the most effective and widely used solar cell. Solar cells in this generation are produced on wafers with each wafer producing 2-3 W of power [18]. Generally, there are two types of first-generation solar cells and they differ by their crystallisation levels. If the wafer is one crystal, then the solar cell is called the single crystal (monocrystalline) solar cell. If the wafer consists of crystals and grains, then the solar cell is a multicrystalline (polycrystalline) solar cell [19-20]. Despite producing much power, this generation of solar cells have a high cost of production [21].

Second-generation solar cells are made from thin films of semiconducting materials as photoactive layers [21]. A thin photoactive layer means that the cost of production is reduced and the material can be deposited for a flexible and semi-transparent solar cell. Solar cells found in this generation are made with semiconductors such as cadmium telluride (CdTe), copper indium gallium selenide (CIGS) and amorphous silicon. Despite the advantages, the solar cells in this generation are limited by their difficulty in manufacturing large quantities as well as their lower efficiencies in comparison to the first-generation solar cells [22-23].

The third-generation solar cells are novel and still growing as they have not yet taken over the solar cell market. However, they show great potential as current solar cell research is dominated by this generation and within a short space of time, significant progress has been made [16]. This generation has a variety of solar cells including nanocrystal based, polymer, perovskite and dye sensitised solar cells [21]. The advantages of these solar cells are characterised by low cost of production, flexibility, lightness and their ever improving efficiencies [24-25]. Generally, these solar cells have low cost of fabrication as compared with those from first and second generation and unfortunately their efficiencies are low. Perovskite solar cells, however, have

© University of Pretoria

efficiencies comparable to solar cells in the previous generations [26]. Despite this, they suffer from chemical and thermal stability [15, 27].

In this study, third-generation solar cells will be fabricated using metallophthalocyanines (MPc) as photoactive layers. This is due to their intense light absorption in the visible to near infrared and they have high chemical and thermal stability compared to the widely used perovskite and polymer photon absorbers. Transition metal dichalcogenides (TMDs) will be employed in this study as charge-carrier agents. These materials are intrinsically n-type (only used as ETL) so they will undergo p-type doping with gold (Au) so that they can also be used as HTL. TMDs have high charge carrier mobility [26-27], this means that they are able, under an electric field, to move electrons and holes quickly through their surface [28]. This implies that the electrons and the holes will not recombine quickly after electron-hole pair generation resulting in an improved performance of the solar cell.

1.2 Problem statement

Energy is a valuable resource and is important in supporting daily processes [29-30]. The rapid increase in population and improvement of technologies has increased the demand for energy and this will eventually lead to the depletion of fossil fuels as they fall under the category of non-renewable energy sources [30–32]. To avoid problems associated with the burning fossil fuels, a reliable, renewable and cost-effective energy source is needed [32].

Figure 1 shows several sources that can be used as alternatives to coal. Sources used to date include natural gas [33], hydroelectricity [3] and nuclear power [33-35].

© University of Pretoria

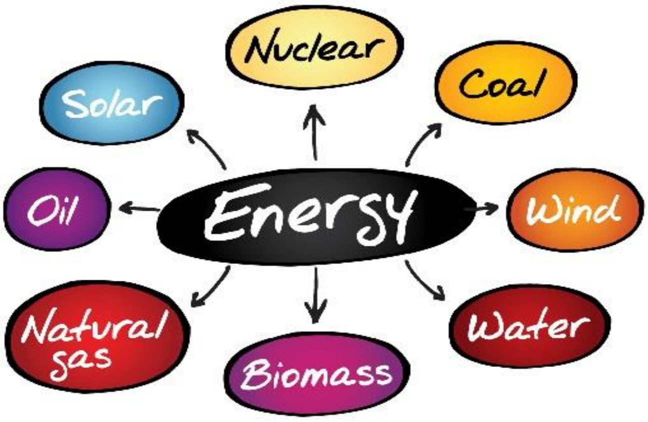

Figure 1: Sources of energy that can be used as alternatives for fossil fuel generated energy [36].

Some of these power sources have drawbacks which make them less competitive to the widely used fossil fuels. For example, if natural gases leak, they pose a dangerous threat to humans and the environment [31, 37]. Hydropower plants, on the other hand, have a negative impact on aqueous ecosystems and settlements near dams [32] while nuclear power has a problem of producing radioactive waste [38]. As a result of these challenges, solar energy has been found to be the best source of energy as it is renewable and clean [13, 26]. This study proposes fabrication of a solar cell using materials that are: structurally flexible, thermally and chemically stable, have enhanced charge separating capabilities and absorb light at visible and near IR region. It is hoped that the solar cell will have improved stability and performance.

1.3 Research questions

- Can photostable MPc's improve light absorption of third generation solar cells?
- Can the use of TMDs improve the performance of third-generation solar cell?
- Can the combination of TMDs and MPc's in a solar cell improve their performance?

© University of Pretoria

1.4 Aims and Objectives

The aim of this work is to fabricate a third-generation solar cell using MPc's as photoactive layers and TMDs as charge carriers to improve cell stability and performance.

In order to achieve the aim, the following objectives are proposed:

i. Synthesise mono to few layer TMDs.
ii. Apply p-type doping to TMDs using gold.
iii. Incorporate the doped and pristine TMDs in metallophthalocyanine-based solar cells as HTL and ETL, respectively.
iv. Characterise the different layers of the solar cells using Raman spectroscopy, scanning electron microscopy (SEM), X-ray diffraction (XRD) and Energy-dispersive X-ray spectroscopy.
v. Test the fabricated solar cells by taking dark and illuminated I-V measurements.

1.5 Significance of the research

The contribution of this research project is to find out if the materials used for fabrication of the solar cells, which are TMDs and MPc's, can improve the performance of the solar cell. The effect of doping and varying the types of MPc's on the performance of the solar cell will be studied.

1.6 Research assumptions

This research assumes that the use of TMDs together with MPc's will improve the stability and performance of third-generation solar cells.

1.7 Research limitations

- Temperature control in TMD synthesis cannot be easily maintained.
- Obtaining a smooth film of MPc's when depositing on glass substrate using the dip coating technique.

© University of Pretoria

1.8 References

[1] L. Hewage, U. Willhelm, and J. W. Mesthrige, “Global research on carbon emissions : A scientometric review,” *Sustainability.,* vol. 2, pp. 1–25, 2019.

[2] F. Perera, “Pollution from fossil-fuel combustion is the leading environmental threat to global pediatric health and equity : Solutions exist,” *Int. J. Environ. Res. Public Health.,* vol. 16. pp. 1-17, 2018.

[3] M. O. Bello, S. A. Solarin, and Y. Y. Yen, “The impact of electricity consumption on CO_2 emission, carbon footprint, water footprint and ecological footprint : The role of hydropower in an emerging economy,” *J. Environ. Manage.*, vol. 219, pp. 218–230, 2018.

[4] M. T. Kibria, A. Ahammed, S. M. Sony, and F. Hossain, “A Review : Comparative studies on different generation solar cells technology,” *Int. Conf. Environ. Asp. Bangladesh.*, pp. 51–53, 2014.

[5] H. Wang, H. Feng, and J. Li, “Graphene and graphene-like layered transition metal dichalcogenides in energy conversion and storage,” *Small*, vol. 10, no. 11, pp. 2165–2181, 2014.

[6] X. Yu and K. Sivula, “Layered 2D semiconducting transition metal dichalcogenides for solar energy conversion,s” *Curr. Opin. Electrochem.*, vol. 2, no. 1, pp. 97–103, 2017.

[7] V. G. Shah and D. B. Wallace, “Low-cost solar cell fabrication by drop-on-demand ink-jet printing low-cost solar cell fabrication by drop-on-demand ink-jet Printing,” *IMAPS 37th Annual International Symposium on microelectronics*, 2015.

[8] Q. Guo, S Jun Kim, M Kar, W. N. Shafarman, R. W. Birkmire, E. A. Stach, R. Agrawal and H. W. Hillhouse., “Development of $CuInSe_2$ nanocrystal and nanoring inks for low-cost solar cells 2008,” *Nano. lett.* vol. 8, no. 9., pp. 2982-2987, 2008.

[9] T. Markvart and E. Sciences, “Principles of solar cell operation.” McEvoy's Handbook of Photovoltaics: Fundamentals and Applications, 2003.

[10] M. Ragoussia and T. Torres., “New generation solar cells: concepts, trends

© University of Pretoria

and perspectives" *Chem. Commun*., vol. 51., pp 3957-3972, 2015.

[11] N. Marinova, S. Valero, and J. L. Delgado, "Organic and perovskite solar cells : working principles , materials and interfaces journal of colloid and interface science organic and perovskite solar cells : working principles , materials and interfaces," *J. Colloid Interface Sci.*, vol. 488, pp. 373–389, 2016.

[12] N. Marinova, S. Valero, and J. Luis, "Organic and perovskite solar cells : Working principles , materials and interfaces," *J. Colloid Interface Sci.*, vol. 488, pp. 373–389, 2017.

[13] J. Shieh, C. Liu, H. Meng, S. Tseng, and Y. Chao, "The effect of carrier mobility in organic solar cells," *J. Appl. Phys*. vol. 107, pp. 1–9, 2010.

[14] Y. Zhu, J. Liu, J. Zhao, Y. Li, B. Qiao, D. Song, Y. Huang, Z. Xu, S. Zhao and X. Xu ., "Improving the charge carrier transport and suppressing recombination of soluble." *materials.,* vol. 11, pp 759-769, 2018.

[15] I. M. Dharmadasa , Y. Rahaq and A. E. Alam1, "Perovskite solar cells : short lifetime and hysteresis behaviour of current – voltage characteristics," *J. Mater. Sci. Mater. Electron.*, vol. 30, no. 14, pp. 12851–12859, 2019.

[16] D. J. Friedman, "Progress and challenges for next-generation high-efficiency multijunction solar cells," *Curr. Opin. Solid State Mater. Sci.*, vol. 14, no. 6, pp. 131–138, 2010.

[17] M. A. Green, "Third generation photovoltaics : solar cells for 2020 and beyond," *Physica E.,* vol. 14, pp. 65–70, 2002.

[18] A. Khatibi, F. R. Astaraei and M. H. Ahmadi., "Generation and combination of the solar cells : A current model review," *Energy Sci Eng.* vol. 7, pp. 305–322, 2019.

[19] W. A. Badawy, "A review on solar cells from Si-single crystals to porous materials and quantum dots," *J. Adv. Res.*, vol. 6, no. 2, pp. 123–132, 2015.

[20] S. Sharma, K. K. Jain, and A. Sharma, "Solar cells : In research and applications -- *A Review," MSA.*, vol. 6, pp. 1145–1155, 2015.

[21] J. A. Luceño-Sánchez, A. M. Díez-Pascual and R. P. Capilla "Materials for

© University of Pretoria

Photovoltaics: State of Art and Recent Development," *Int. J. Mol. Sci.*, vol. 20, pp. 967-1018, 2019.

[22] Y. Farré, L. Zhang, Y. Pellegrin, A. Planchat, E. Blart, M. Boujtita, L. Hammarström, D. Jacquemim, F. Odobel,, "Second generation of diketopyrrolopyrrole dyes for NiO-based dye-sensitized solar cells," *J. Phys. Chem. C.*, *vol. 120.,* pp. 7923−7940, 2016.

[23] O. Vigil-Gala, M. Courel, J. A. Andrade-Arvizu, Y. Sanchez, M. Espındola-Rodrıguez, E. Saucedo, D. Seuret-Jimenez, M. Titsworth, "Route towards low cost-high efficiency second generation solar cells : current status and perspectives," *J Mater Sci: Mater Electron,* vol. 26, pp. 5562–5573, 2015.

[24] J. Yan and B. R. Saunders, "RSC Advances comparison of polymer : fullerene, hybrid polymer," *RSC Adv*.,Vol. 4, pp. 43286–43314, 2014.

[25] S. Ananthakumar, J. R. Kumar and S. M. Babu "Third-Generation solar cells : concept , materials and performance - An Overview.", *Environmental Chemistry for a Sustainable World,* vol. 23, pp. 306-339, 2019.

[26] W. Ke and M. G. Kanatzidis, "Prospects for low-toxicity lead-free perovskite solar cells," *Nat. Commun.*, vol. 10, pp. 1–4, 2019.

[27] Y. Zhou and Y Zhao "Chemical stability and instability of inorganic halide perovskites," vol. 12, no. 1, pp. 1495–1511, 2019.

[28] R. Singh, A. Giri, M. Pal, K. Thiyagarajan, J. Kwak, J. Lee, U. Jeong and K. Cho., "Perovskite solar cells with an MoS_2 electron transport layer," *J. Mater. Chem. A*, vol. 7, pp. 7151–7158, 2019.

[29] X. Li and H. Zhu, "Two-dimensional MoS_2 : Properties, preparation, and applications," *J. Mater.*, vol. 1, no. 1, pp. 33–44, 2015.

[30] A. A. Tedstone, D. J. Lewis, and P. O. Brien, "Synthesis , properties , and applications of transition metal-doped layered transition metal dichalcogenides," *Chem. Mater.,* vol. 28, pp. 1965−1974, 2016.

[31] Y. Wu, F. Zhao, S. Liu, L. Wang, L. Qiu, G. Alexandrov and V. Jothiprakash., "Bioenergy production and environmental impacts," *Geosci. Lett.*, vol. 5, no. 1, 2018.

© University of Pretoria

[32] X. Liao and X. (Roc) Shi, "Public appeal, environmental regulation and green investment: Evidence from China," *Energy Policy*, vol. 119, pp. 554–562, 2018.

[33] K. Dong, R. Sun, and X. Dong, "CO_2 emissions, natural gas and renewables, economic growth: Assessing the evidence from China," *Sci. Total Environ.*, vol. 640–641, pp. 293–302, 2018.

[34] F. Ye, F. Wang, C. Meng, L. Bai, J. Li, P. Xing, B. Teng, L. Zhao, S. Bai, "Crystalline phase engineering on cocatalysts: A promising approach to enhancement on photocatalytic conversion of carbon dioxide to fuels," *Appl. Catal. B Environ.*, vol. 230, no. 2010, pp. 145–153, 2018.

[35] N. J. Jeon, J. H. Noh, Y. C. Kim, W. S. Yang, S. Ryu, and S. Il Seok, "Solvent engineering for high-performance inorganic-organic hybrid perovskite solar cells," *Nat. Mater.*, vol. 13, no. 9, pp. 897–903, 2014.

[36] N. Roslan, M. E. Ya'acob, M. A. M. Radzi, Y. Hashimoto, D. Jamaludin, and G. Chen, "Dye sensitized solar cell (DSSC) greenhouse shading: New insights for solar radiation manipulation," *Renew. Sustain. Energy Rev.*, vol. 92, pp. 171–186, 2018.

[37] E. P. Anderson, M. C. Freeman, and C. M. Pringle, "Ecological consequences of hydropower development in central america : impacts of small dams and water diversion on neotropical stream fish assemblages," *River Res. Applic.*, vol. 411, pp. 397–411, 2006.

[38] R. J. Budnitz, H. Rogner, and A. Shihab-eldin, "Expansion of nuclear power technology to new countries – SMRs , safety culture issues , and the need for an improved international safety regime," *Energy Policy*, vol. 119, pp. 535–544, 2018.

© University of Pretoria

Chapter 2: Literature review

2.1 Overview

Graphene is a 2D layered semiconducting material made up of carbon atoms hexagonally bonded to each other [1-2]. After its discovery in the 2000s, graphene has been used in many applications and fields due to its favourable properties. Graphene possesses properties such as high surface area, high charge transfer mobility and high chemical tolerance [3]. Graphene is a semiconductor with a zero band gap making it ohmic and highly conductive [3]. These desired properties encouraged researchers into studying other 2D layered semiconducting materials. Examples of these 2D materials are transition metal dichalcogenides (TMDs), hexagonal boron nitride (hBN) and other layered oxides. This study will be focusing on the synthesis and characterisation of TMDs, specifically WS_2 and MoS_2, for solar cell application.

2.1.1 Transition metal dichalcogenides

Transition metal dichalcogenides are semiconducting materials with the molecular formula MX_2, were M is a transition metal (Mo, W, Sn, etc) and X a chalcogen (S, Se, Te) [4–6]. For each TMD, the layer of M atoms is sandwiched between two layers of X atoms and these layers are held together by covalent bonds. TMDs naturally occur as bulk materials which simply means that many layers of MX_2 are held together by weak van der Waals forces. In this bulk form, these materials have a band gap of ~1.2 eV [7–9]. When bulk, TMDs can be converted to mono or few layers by separating the nanosheets. The band gap then changes to ~1.8 eV [6,10-11]. TMDs have interesting properties such as high surface area [12], catalytic active sites [13] and the band gap can be manipulated [14]. These properties have led to TMDs being used in a variety of applications such as solar cells [5], lubricants [15], transistors [16] and hydrogen evolution catalysis [16].

Figure 2.1 shows that TMDs have two possible geometries, the trigonal prismatic (2H-MX_2) and the octahedral phase (1T-MX_2) [17].

© University of Pretoria

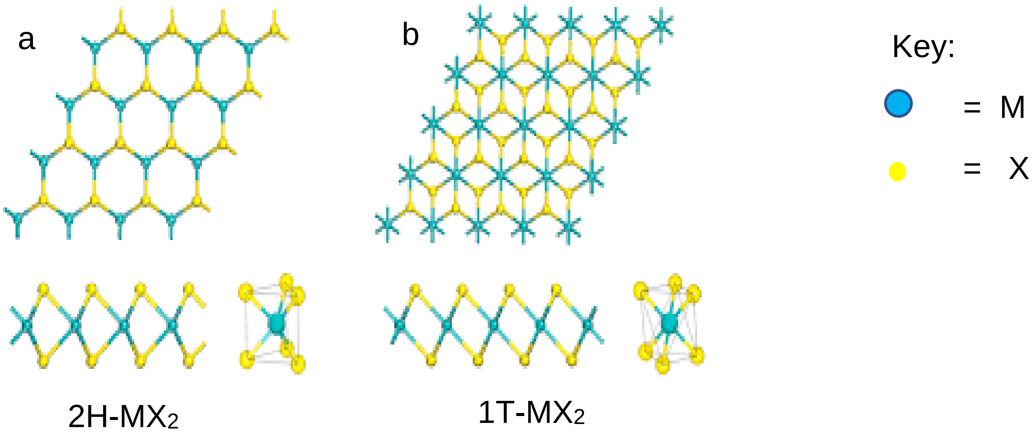

Figure 2.1: TMD geometries, (a) the trigonal prismatic geometry (2H-MX_2) and (b) the octahedral geometry (1T-MX_2)[17].

Materials with the 2H geometry are semiconducting while those with the 1T geometry are metallic [18]. The 2H-MX_2 has a transition metal atom in each nanosheet bonded to six X atoms in a prism-like fashion (prismatically) [9]. This is the thermodynamically stable phase of this material at room temperature [17]. In the 1T-MX_2 geometry, the metal atom is coordinated to six X atoms in a distorted octahedral manner [17]. This phase is metastable which means that the material is thermodynamically stable only when subjected to deliberate disturbances. For certain applications, such as hydrogen evolution reactions, the 1T geometry is preferred, hence the need to convert 2H-MX_2 to 1T-MX_2 is necessary. Intercalation with atoms such as lithium and potassium has been reported to achieve this conversion [19]. However, the material will revert to the 2H-MX_2 configuration due to thermodynamic instability of the 1T-MX_2 geometry.

Several techniques can be used to identify the different phases of TMDs. An example is Raman spectroscopy. The Raman spectra for TMDs are characterised by the E^1_{2g} and A_{1g} peaks at ~385 cm^{-1} and 420 cm^{-1}, respectively. When comparing the Raman spectra of the two geometries, additional peaks are observed for the 1T geometry. These peaks are known as the J_1, J_2 and J_3 and are observed at ~160 cm^{-1}, ~230 cm^{-1} and ~330 cm^{-1}, respectively [6]. The other technique that can be used to identify TMD geometry is X-ray photoelectron spectroscopy (XPS) [20]. XPS can also be used for quantitative analysis of the 1T-MX_2 and the 2H-MX_2. Consider XPS scan of Mo element in the 3d region. Mo 3d exhibits only two peaks. The first peak observed at binding energy of 220 eV corresponds to Mo^{4+} $3d_{5/2}$ and the second peak is observed at the binding energy of 232 eV and corresponds to Mo^{4+} $3d_{3/2}$. However, for 1T-MX_2,

© University of Pretoria

the Mo^{4+} $3d_{5/2}$ electrons are found to be responsible for a peak at the binding energy of 228.1 eV and the Mo^{4+} $3d_{3/2}$ electrons being responsible for a peak at the binding energy of ~231.1 eV. For 2H-MX_2, the Mo^{4+} $3d_{5/2}$ electrons are found to be responsible for a peak at the binding energy of 229.5 eV and the Mo^{4+} $3d_{3/2}$ electrons are responsible for a peak at the binding energy of ~232.1 eV. Deconvolution of the peaks gives the relative concentrations of the two phases [20]. All these is clearly demonstrated by figure 2.2 below.

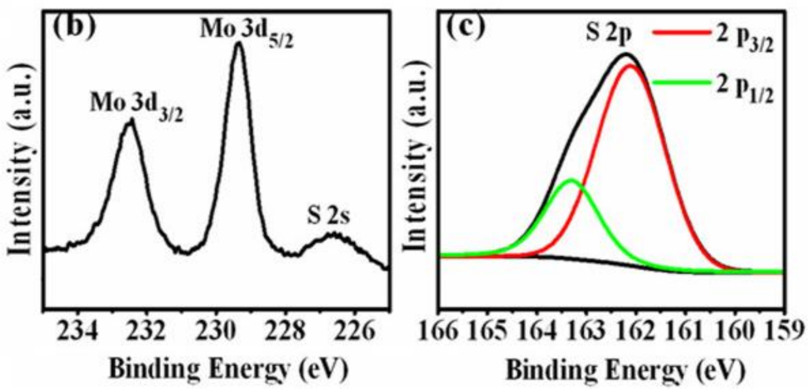

Figure 2.2: High-resolution XPS spectra of (b) Mo 3d and (c) S 2p for the exfoliated MoS_2 nanosheets [20].

2.1.2 TMD exfoliation

As required for the synthesis of all the nanomaterials, TMD synthesis can either be achieved through a bottom-up or a top-down synthesis technique. Bottom-up synthesis involves starting with the precursors or atoms that react and build up to form the final, desired product. Examples of bottom-up approach techniques employed for the synthesis of TMDs are atomic layer deposition, vapour generation and chemical vapour deposition [4].

On the other hand, top-down synthesis include techniques that focus on overcoming the van der Waals forces between the nanosheets in bulk materials. This leads to the separation of TMD layers to obtain few layered nanosheets. This process is known as exfoliation. Several techniques can be used to achieve this process, examples include micromechanical exfoliation, liquid-mediated exfoliated and chemical intercalation and exfoliation. The liquid-mediated exfoliation is the best way to synthesize TMDs as it yields TMDs which are scalable [21] and in high yields [22-23].

© University of Pretoria

Bernal and Milano (2016) synthesised several TMDs through a liquid-assisted exfoliation method using a variety of solvents [22]. They concluded that for this technique to be effective, the solvent used must have a surface tension that matches that of the TMD to be exfoliated. Solvents that match the surface tension of TMDs are those with high boiling points. They concluded that the best solvent for TMD exfoliation is N-methyl-2-pyrrolidone (NMP) [22]. Gupta and Vasudevan (2016) investigated the chemical stability of NMP exfoliated MoS_2 [24]. The chemical stability studied, compared TMDs exfoliated in dry NMP and NMP containing traces of water. The conclusion drawn from this study was that the traces of water increases chemical stability [24]. Backer *et al.* (2016) synthesised TMDs using liquid assisted exfoliation [24]. Since this technique yields polydispersed TMDs of different layers, post exfoliation size selection techniques are required to yield a specific number of layers depending on the application. For example, large and thin TMDs nanosheets are required for electronics as they are more flexible, while small and lateral TMDs are required for catalysis. As such, it is necessary to do a specific post exfoliation size selection technique to yield desired TMDs for specific applications [25]. These studies confirm that the best way to synthesise TMD nanosheets is through liquid-assisted exfoliations.

Liquid-mediated exfoliation is an exfoliation technique that requires the use of a solvent under ultrasonic conditions. This technique employs the generation of energy from vibrational forces to isolate layers [26]. This exfoliation uses pressure of vibrations from the ultrasonicator to produce energy that aid in exfoliation. The energies produced can be categorized into vibrational modes and caviation forces [27-28]. Continuous exposure of bulk TMD to these conditions leads to continual exfoliation and the dispersed nanosheets are obtained from the bulk unexfoliated material *via* centrifugation. This method is also called ultrasonic exfoliation as it uses ultrasonic baths or probes to create ultrasonic energies as vibrations and caviations which are transmitted to the sample. Exfoliation can only occur if the ultrasonic energy produces vibrations that are high enough to overcome the weak van der Waals forces holding the bulk TMD in place [29]. Exfoliation also depends on the exfoliation time [30]. Longer exfoliation periods result in complete exfoliation of bulk TMDs into 2D TMDs (monolayer). Figure 2.3 illustrates the process of TMDs exfoliation through a liquid-assisted sonication method. This figure clearly illustrates that sonication energy

© University of Pretoria

is as an important factor as the solvent choice and exfoliation time and if these factors are chosen poorly, the material will restack after exfoliation [30].

Caviation forces, on the other hand, carry more energy than vibrational forces and are able to efficiently exfoliate bulk TMDs at shorter time periods [26]. As reported by Bernal and Milano (2016), a good solvent has its surface tension matching the TMD's [22]. As such, when a good solvent is used for a relatively longer time, the sheets will remain separated with the opposite leading to restacking of the sheets.

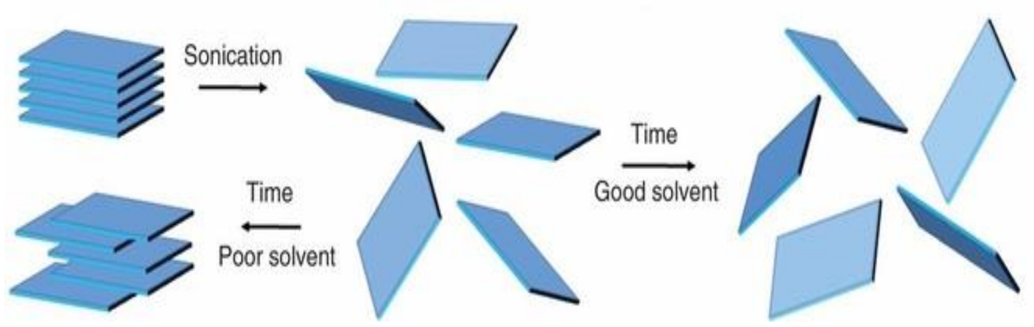

Figure 2.3: A schematic diagram illustrating the influence of time and solvent type on TMD exfoliation from bulk form [30].

As previously stated, the exfoliation of bulk TMD to mono/few layered TMD results in a band gap increase. Bulk TMDs have an indirect band gap whereas few layered TMDs have a direct band gap. An indirect band gap is where the highest point of the valence band is not vertically aligned with the lowest point of the conduction band whereas a direct band gap is where the highest point of the valence band is vertically aligned with the lowest point of the conduction band. To fully understand this phenomenon, one has to look at the Brillouin zone.

The Brillouin zone is a primitive cell in reciprocal space. It is an allowed energy of electrons in momentum space. Γ, M and K represent symmetry points in the Brillouin zone. The Brillouin zone of TMDs can be represented in a diagram where Γ is at the centre of the Brillouin, M is at the centre of the edge and K is at the corner point. The allowed energy levels of electrons are quantized and the paths along the high symmetry points (Γ, M and K) are used as the x coordinates in the band structure diagram. The difference between the highest point of the valence band and the lowest point of the conduction band is called the band gap [31, 32]. Figure 2.4 shows the band structure of a TMD upon transition from bulk to monolayer.

© University of Pretoria

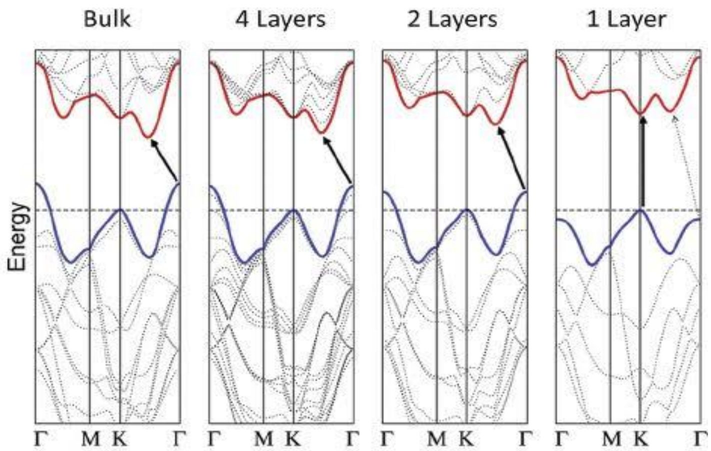

Figure 2.4: Band gap transitions from bulk to monolayer TMD [30].

From Figure 2.4, it can be observed that the vertical axis of the band structure is the energy and the horizontal axis is the real space represented by high symmetry points. The band structure of the bulk shows the highest point (maximum) of the valence band situated on the Γ point of the Brillouin zone and the lowest point (minimum) of the conduction band is located between the K point and the Γ point of the Brillouin zone. This point is referred to as the T point (the median K point and the Γ point). The excitonic transition energy (the band gap) between the two points is ~1.2 eV. Since the two points are not vertically aligned, the resulting band gap is called an indirect band gap [33-34]. At the K point of the bulk structure, the sub minimum of the conduction band is vertically aligned with the sub maximum of the valence band. The distance between the two points is ~1.8 eV [30].

Upon exfoliation, the excitonic transition energy at the K point of the Brillouin zone does not change (remains ~1.8 eV). Meanwhile, the distance between the two points that were making the indirect band gap (the section of the valence band located at Γ point and the section of the conduction band located at the T point of the Brillouin zone) increases monotonically [35]. This implies that after exfoliation, the highest point of the valence band and the lowest point of the conduction band are vertically aligned at the K point of the Brillouin zone. As such, points making the band gap are vertically aligned and the resulting band gap is a direct band gap which has a value of ~1.8 eV [30, 33–35]. Figure 2.5 summarises the excitonic processes that occur at the band gaps of bulk (indirect band gap) and 2D (direct) TMDs.

© University of Pretoria

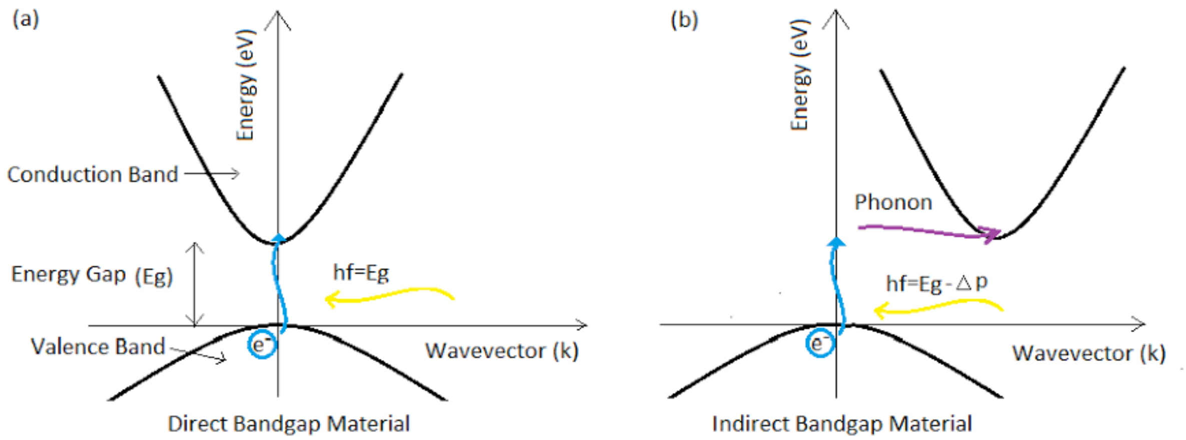

Figure 2.5: A schematic representation of excitonic transitions that take at a (a) direct band gap and (b) indirect band gap semiconductor [36].

Depending on the application of TMDs, it is mandatory to assess which type of band gap is preferred. In this study, TMDs will be used for solar cell application. Solar cell processes start with the absorption of light and excitation of the electron from the valance band to the conduction band, leaving a hole behind. However, based on the electronic structure of bulk TMD (Figure 2.5b), since it is indirect, its application will mean the electron will not be in the conduction band after absorption of photon and excitation of an electron. This is because, as stated above, the lowest level of the conduction band is not aligned with the highest level of the valence band. As such, a phonon is additionally required to provides the electron with angular momentum to travel horizontally in the band gap as the photon energy only powers the vertical motion of the electron. This simply means that for an electron to be excited from the valence band to the conduction band in a bulk TMD, a photon of energy is required to move the electron vertically to the minimum level of the conduction band, followed by phonon energy which will give the electron the momentum energy to move horizontal to the actual position of the minimum in the conduction band.

On the other hand, with 2D TMDs' electronic structure (Figure 2.5a), since the lowest point of the conduction band is aligned vertically above the highest point of the valence band, only the energy from the photon will be required to excite an electron to the conduction band and no phonon energy is needed. As a result, since sunlight only

© University of Pretoria

provides photons, a direct band gap is advantageous for solar cell application over indirect band gap hence the exfoliation of TMDs into 2D nanosheets is essential.

Exfoliation of TMDs can be confirmed by different characterisation techniques. All these techniques involve comparison of the data taken when the material was still in bulk form and the data after exfoliation has taken place. Techniques employed in this study to confirm exfoliation are Raman spectroscopy, SEM and XRD.

2.1.3 TMD doping

Doping is a process whereby impurities are intentionally introduced into an intrinsic semiconductor for the purpose of manipulating its electrical, optical and structural properties [36]. This occurs using a dopant which is simply a foreign species with a different number of valence electrons [37–39]. The dopant either has one more or one less valence electron as compared to the intrinsic semiconductor depending on the desired electrical conductivity.

There are two types of doping procedures for semiconductors, namely p-type and n-type doping. Dopants that accept surplus electrons from the original material are called acceptors and cause p-type doping [37-38]. These dopants have less valence electrons than the species being doped (the semiconductor). Consider a silicon semiconductor undergoing p-type doping. A silicon atom has four valence electrons and replacing one atom with any element that has three valence electrons, such as boron, will make the semiconductor p-type as there will be fewer electrons and more positive holes hence the term p-type [40].

Dopants that donate electrons to the original material are called donors and result in n-type doping. These dopants have more valence electrons than the intrinsic semiconductor. Using silicon semiconductor as an example again, replacing one silicon atom with any element with five valence electrons, such as phosphorus will make the semiconductor n-type as there will be more electrons and fewer holes hence the term n-type [40].

Doping manipulates the electronic properties of a semiconductor by shifting the position of the fermi level [40]. Figure 2.6 illustrates the location of the fermi level in the band gap of a semiconductor when it undergoes (a) n-type and (b) p-type doping

© University of Pretoria

[41]. The figure shows that n-type doping shifts the fermi level upwards towards the conduction band (Figure 2.6a).On the other hand, when a semiconductor undergoes p-type doping the fermi level shifts downwards towards the valence band (Figure 2.6b) [41-42].

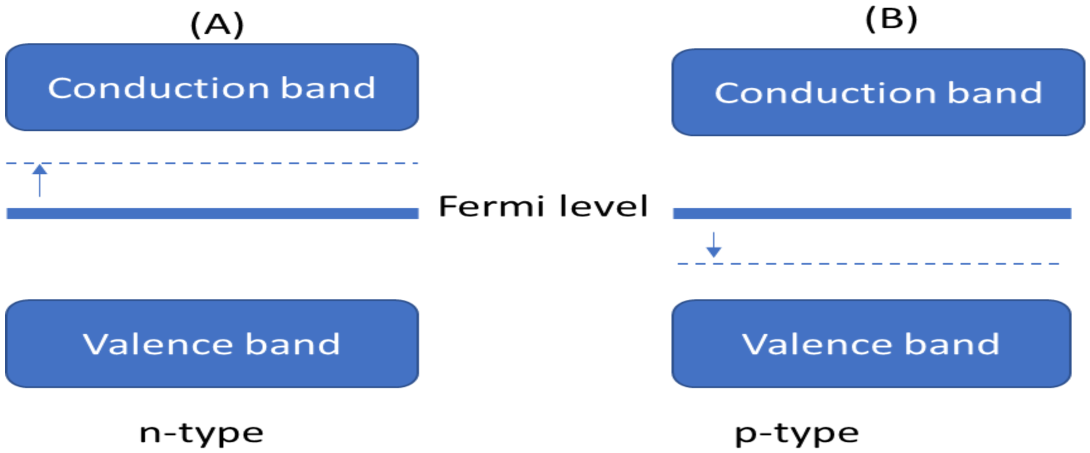

Figure 2.6: An illustration of fermi level shift upon (a) n-type and (b) p-type doping [41].

There are two ways in which TMDs and other semiconductors can undergo p or n-type doping. The first way is called substitutional doping, where the M or the X atom in the TMD honeycomb structure gets replaced by a foreign species with a different number of valence electrons. The resulting doped TMD is stable as the dopant species is covalently bonded [37-38, 42]. This type of doping is irreversible [38, 43].

The second doping procedure is called surface charge transfer. It involves the adsorption of a foreign species on the surface of the TMD semiconductor leading to exchange of electrons between the adsorbed dopant and the TMD [46-47]. This type of doping is reversed as soon as the dopant desorbs from the surface of the TMD. Surface charge transfer relies heavily on the relative alignment of the dopant HOMO/LUMO with the fermi level of the TMD [48]. When the fermi level of the TMD is below the HOMO of the dopant, electrons will flow from the dopant to the TMD. Such a dopant is called a donor, and this is n-type doping [49]. When the fermi level of the TMD is above the LUMO of the dopant, electrons will flow from the TMD to the dopant. Such a dopant is called an acceptor, and this is p-type doping [50].

© University of Pretoria

Mouri *et al* (2013) investigated the effect of p-type and n-type doping on TMD photoluminescence. The n-type dopant was a biochemical molecule NADH while the p-type dopants were tetracyanoquinodimethane (TCNQ) and 2,3,5,6-tetrafluoro-7,7,8,8-tetracyanoquinodimethane (F_4TNCQ). Conclusions drawn from this study that p-type doping enhanced photoluminescence which is a desired property [51].

Zhu *et al.* (2017) studied the effects of doping MoS_2 nanosheets with V, Nb and Ta. Several properties and applications of the materials were investigated upon doping. The doped materials exhibited greater catalytic stability which was attributed to the strong bonds between the S vacancies and the dopant atoms [43]. The gas adsorption properties of doped MoS_2 were also studied. The doped material showed improved adsorption and sensitivity [43]. This doping procedure on MoS_2 is meant to improve its electrocatalytic activity towards hydrogen evolution reaction and oxygen reduction reaction. Zhu *et al*. (2017) encouraged Chia *et al.* (2018) to examine the doping effect on the electrocatalytic properties of WSe_2. Doping of WSe_2 with V, Nb and Ta resulted in the TMD having improved electrocatalytic efficiency towards hydrogen evolution reaction and oxygen reduction reaction. Active sites were also increased as evidenced by morphological changes from thick bulk pieces to thinner doped fragments [43].

Fu *et al.* (2017) applied p-type doping on tungsten TMDs using Ta. The influence that this type of doping had on the material was investigated. Upon WSe_2 doping, the newly formed material exhibited competitive p-type performance when applied in field effect transistors (FET) which includes ~10^{-6} current on/off ratio at room temperature. The material further showed excellent photo detecting performances as compared to undoped WSe_2 [38].

Despite TMDs being n-type semiconductors, they can still undergo n-type doping. Upon undergoing this type of doping, TMDs will have an enforced n-type character as the fermi level will be shifted further upwards towards the conduction band. This type of doping usually leads to materials with improved properties such as adsorption capabilities [52]. An example of such is the n-type doping of monolayer MoS_2 by p-toluene sulfonic acid as reported by Andleeb *et al.* (2015). The enforced n-type property was identified and the material was used a transistor and it was found that as time increased, the threshold voltage shifted to a more negative value suggesting that the material became “more” n-type as compared to the pristine material [53]. These

© University of Pretoria

reports show that doping of TMDs can unlock valuable properties which add value to the field of electronics.

There are several techniques that can be used to characterise doped TMDs. These techniques provide information such as the type of doping and identify the dopant. Qin *et al*. (2014) doped MoS_2 nanosheets with nitrogen and characterisation of the doped material was performed using XPS which identified Mo-N bonds confirming the substitution of S atoms by N atoms [45].

Doping TMDs with gold has been reported to convert the material to a p-type semiconductor and also enhance some properties which improve TMD performance in various applications. Liang *et al*. (2009) subjected MoS_2 to Au doping. With the help of Hall effect measurements, they were able to confirm that the material exhibits p-type semiconducting character [54]. Lin *et al.* (2014) doped MoS_2 with Au and observed that doping improved the chemical reactivity by increasing the number of catalytic sites. From their study, they further concluded that Au doping of MoS_2 improves performance in biosensing and imaging applications [55]. A theoretical study of Au doping on MoS_2 was conducted by Wang *et al*. (2019), the conclusion drawn was that upon doping, the material showed a significant change in the electronic structure and properties which included a reduction in the band gap. Consequently, this led to an enhanced chemical reactivity of the material in comparison with the undoped MoS_2 monolayer. Furthermore, Au-MoS_2 exhibited improved adsorption capacity to the H_2O molecule [55].

Zeng *et al*. (2017) fabricated a Au-WS_2/p-Si electrode for photocatalysis. They concluded that the addition of Au-WS_2 to the electrode provides efficient charge separation and protection for the silicon layer. This implies that Au-WS_2 improved photocatalytic efficiency and stability of the photoelectrode [56].

2.1.4 TMD uses in solar cell applications

TMD nanosheets have been used in several electronic applications. An example of such applications is solar cells. Li *et al.* (2015) fabricated an ultrathin p-n junction using p-type and n-type MoS_2. The p-type MoS_2 was obtained from doping MoS_2 with gold [58]. The fabricated p-n junction device showed solar to electricity conversion for MoS_2

© University of Pretoria

with thicknesses that are less than 8 nm. The film thickness that gave the most efficiency was found to be 3 nm. It was further concluded that ultrathin films were desired since they were flexible, light and transparent, an advantage over the most widely used silicon semiconductor [58]. Gu *et al.* (2013) used ultrathin MoS_2 nanosheets as hole transporting layers in an organic solar cell. The fabricated organic solar cell showed an improved power conversion efficiency (PCE) when compared to the device that used traditional MoO_3 as the hole transporting layer [59]. Tsui *et al.* (2014) fabricated a p-n junction using monolayer MoS_2 and p-Si. The p-n junction demonstrated a power conversion efficiency of 5.23% which is the highest efficiency for TMDs [60]. Xu *et al.* (2019) devised a solar cell with a set up imitating the one reported by Tsui *et al.* (2014). Xu and crew fabricated a device with a large area MoS_2 synthesised through a sol-gel method. Their main aim was to study the effect that MoS_2 had on the heterojunction and the conclusion drawn was that upon the introduction of MoS_2 into the device, the power conversion efficiency increased drastically from 1.1% to 4.6% [61].

Lin *et al.* (2019) fabricated a solar cell with poly[(2,6-(4,8-bis(5-(2-ethylhexyl-3-fluoro)thiophen-2-yl)-benzo[1,2-b:4,5-b']dithiophene))-alt-(5,5-(1',3'-di-2-thienyl-5',7'-bis(2-ethylhexyl)benzo[1',2'-c:4',5'-c']dithiophene-4,8-dione) : phenyl-C61-butyric acid methyl ester (PBDB-T-2F:PCBM) combined with WS_2 as the electron transporting layer. The solar cell yielded a percentage coefficient efficiency of 17%. This PCE is the highest reported for organic solar cells to date [62].

There is a type of junction called a p-*i*-n junction. It consists of an intrinsically undoped semiconductor sandwiched between the n-type and the p-type semiconductor. This layer helps facilitate charge transport from the p and n-type region, making the diode operate fast and efficiently. Thilagam (2016) fabricated a p-*i*-n solar cell with the WS_2/MoS_2 heterostructure situated at the *i* region. Figure 2.7 shows possible ways that band structures of two semiconductors can align if the semiconductors are put in contact. Figure 2.7a shows a straddling gap (type I) which occurs when semiconductor A (SC A) and semiconductor B (SC B) are put into contact. This results in a band alignment that has the conduction band of SC A being higher than the conduction band of SC B and the valence band of SC A being lower than the valance band of SC B. Figure 2.7b shows another possible alignment type that can occur when two semiconductors are put into contact. This type of alignment is called the staggered

© University of Pretoria

gap (type II) which occurs when the conduction band of SC A is higher than the conduction band of SC B, on the other hand, the valence band of SC A having the energy that is between the conduction and the valence band of SC B. Lastly, Figure 2.7c shows the other possibility of band alignment called the broken gap (Type III). This band alignment arises when both the conduction and the valance band of SC A are higher than the conduction band of SC B [64]. The band alignment between MoS_2 and WS_2 is a staggered type (type II). This creates a driving force for effective charge separation consequently enhancing the performance in solar cells. The charge separation at the *i* region leads to electrons moving to the MoS_2 while holes move to the WS_2 layer of the heterostructure [63].

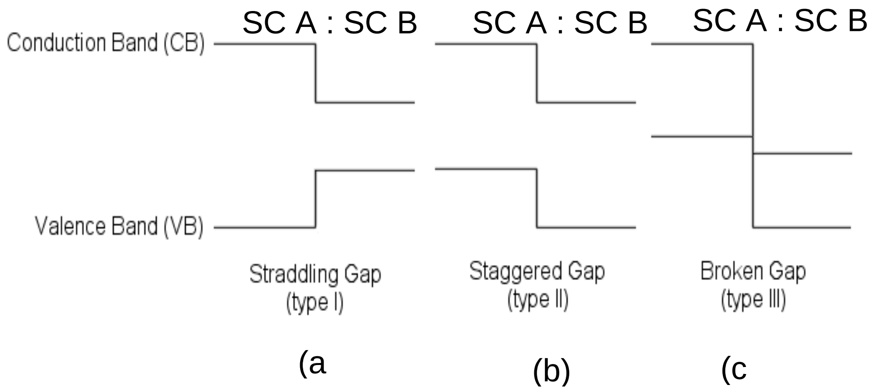

Figure 2.7: A schematic illustration of (a) type I band alignment, (b) type II alignment and (c) type III alignment of band gaps when two different semiconductors are put in contact [64].

2.2. Phthalocyanines (Pcs)

The first report of a phthalocyanine was in 1907 at the South Metropolitan Gas Company, London [65]. Pcs were synthesised accidentally in the process of trying to prepare o-cyanobenzamide. The material was identified as a blue and insoluble compound. Two decades later (1927) at Fribourg University, the reaction of 1,2-dibromobenzene with copper cyanide yielded copper phthalocyanine, which was described as a highly stable blue material [66]. In 1928 at the Grangemouth plant of Scottish Dyes Ltd, copper phthalocyanine, and copper naphthalocyanine, were, accidentally synthesised while trying to synthesise phthalimide from phthalic anhydride [65, 67]. Researchers were amazed by the thermal and chemical stability

© University of Pretoria

exhibited by their newly formed material but did not characterise the material. The materials were named Scottish dyes [65]. It was not until 1933 when the term phthalocyanine was first coined. This term was derived by R.P. Linstead from Greek terms "*naphtha*" which means rock oil and "*cyanine*" which means dark blue. Due to academic interest, Linstead studied and investigated the material thoroughly until he elucidated its structure and determined its chemical properties [65-67].

2.2.1 Properties of phthalocyanines

Phthalocyanines are highly conjugated organic compounds. Their main application after discovery was their use as colourants [68]. They are characterised as aromatic and macrocyclic compounds which are made up of four isoindole groups connected by nitrogen atoms as shown in Figure 2.8. Metal free Pcs are denoted as H_2Pc (Figure 2.8a) have an oxidation state of Pc^{-2}. However, oxidation and reduction can still occur on the H_2Pc [69].

The phthalocyanine molecule contains 18-π electrons and the delocalisation of these electrons renders them useful for various applications such as solar cells and other opto-electronic devices [70]. Phthalocyanines are chemically and thermally stable [71–73]. The structure of the phthalocyanines can be modified and this makes room for molecular engineering of its physical properties. As shown by Figure 2.8b, phthalocyanines can be substituted at the centre by a metal atom. Approximately ~70 different metal atoms can be incorporated at the centre of the ring. Upon incorporation, new properties arise and different properties are observed for different metal atoms [74-75]. When phthalocyanine are substituted at the centre by a metal atom, they are referred to as metallophthalocyanines (MPc's).

© University of Pretoria

a) b)

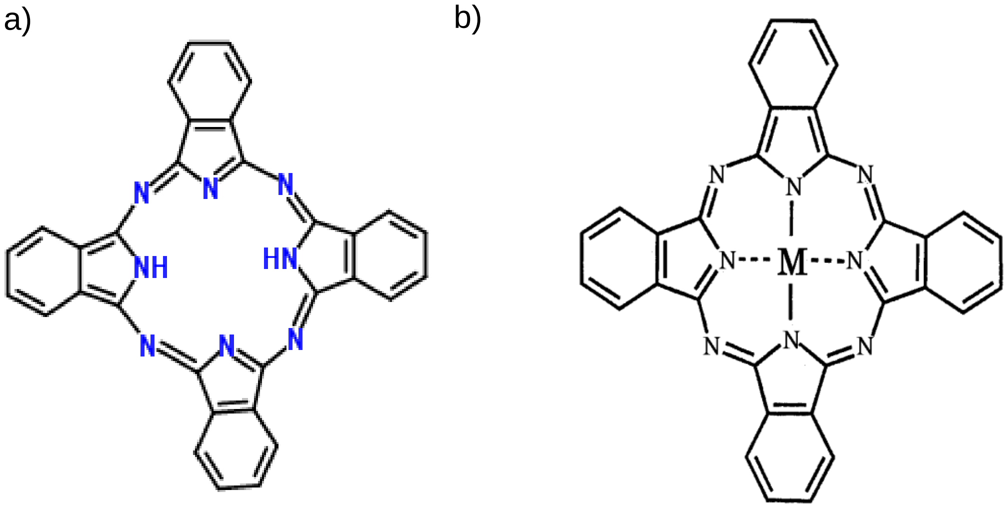

Figure 2.8: The chemical structure of a (a) metal free phthalocyanine (H_2Pc) and b) metallophthalocyanine (MPc). M represent the central metal atom [76].

2.2.2 Application of metallophthalocyanines (MPc’s) in solar cells

This study aims to utilise various MPc’s as photoactive layers for solar cell application. There are several requirements that a material needs to meet in order to be a good photoactive layer in a solar cell device. Metallophthalocyanines possess preferred properties to be considered for utilisation as photoactive layer of a solar cell [77]. MPc’s exhibit an intense absorption of light in the visible and near IR (550-700 nm). They also absorb light at the UV and low wavelength visible region of the electromagnetic radiation (300-400 nm). This shows that they can absorb enough visible spectra from sunlight to generate the electron-hole pair.

Kim *et al*. (2009) fabricated a number of MPc-based solar cells. The photoactive layers of these solar cells were a blend of MPc and PTCBI (MPc/PTCBI). The PdPc based solar cell showed the highest efficiency as it reached a PCE of 1.3%. An explanation provided for this result was that PdPc had the longest excitonic diffusion as compared to the other MPc’s (ZnPc and CuPc). The results for PdPc-based solar cells showed drastic enhancement of performance when PTCBI was substituted by C_{60} fullerenes. The PCE nearly doubled, as it was reported to be 2.2% [78].

Stakhira *et al*. (2010) fabricated a p-n junction device based on NiPc/ZnO. They compared the performance of the solar cell with the reference single junction Schottky barrier (ITO/NiPc/Al). They reported that the resulting solar cell had a higher PCE

© University of Pretoria

which was 2.5 times higher than the reference device [79]. El-Nahass *et al*. (2003) studied the photovoltaic properties of NiPc/p-Si heterojunction, the resulting solar cell was found to have a PCE of 1.1% [80].

There are several reports where TMDs have been used with phthalocyanines in optoelectronics. Pak *et al*. (2015) reported that a CuPc/MoS_2 heterostructure demonstrated a highly enhanced photo sensitivity of a field effect transistor (FET) as compared to an FET made of only MoS_2. This improvement of performance was attributed to a p-n junction between the two materials which was not prone to oxygen adsorption leading to reduced electron-hole recombination rates [81]. This implies that the resulting device is a good photon absorber with low electron-hole recombination rates.

In this work, MPc's will be used together with TMDs to fabricate a solar cell which is a good photon absorber and limited electron-hole recombination processes. The fabricated solar cells will have high charge transfer that occurs immediately after electron-hole generation. These properties will boost the performance of the proposed solar cells.

© University of Pretoria

2.3 References

[1] H. Wang, H. Feng, and J. Li, "Graphene and graphene-like layered transition metal dichalcogenides in energy conversion and storage," *Small*, vol. 10, no. 11, pp. 2165–2181, 2014.

[2] T. Radadiya, "A properties of graphene," *EJMSE.,* vol. 2, No.1, pp.6-18, 2015.

[3] C. A. Ubani, M. A. Ibrahim, M. A. M. Teridi, K. Sopian, J. Ali, and K. T. Chaudhary, "Application of graphene in dye and quantum dots sensitized solar cell," *Sol. Energy*, vol. 137, pp. 531–550, 2016.

[4] J. R. Brent, N. Savjani, and P. O'Brien, "Synthetic approaches to two-dimensional transition metal dichalcogenide nanosheets," *Prog. Mater. Sci.*, vol. 89, pp. 411–478, 2017.

[5] X. Yu and K. Sivula, "Layered 2D semiconducting transition metal dichalcogenides for solar energy conversion," *Curr. Opin. Electrochem.*, vol. 2, no. 1, pp. 97–103, 2017.

[6] R. Lv. J. Robinson, R.E. Schaak, D. Sun and Y.Sun "Transition metal dichalcogenides and beyond: Synthesis, properties, and applications of single- and few-layer nanosheets," *Acc. Chem. Res.*, vol. 48, no. 1, pp. 56–64, 2015.

[7] A. Ambrosi, "Lithium intercalation compound dramatically influences the electrochemical properties of exfoliated MoS_2," pp. 605–612, 2014.

[8] W. Choi, N. Choudhary, G. H. Han, J. Park, D. Akinwande, and Y. H. Lee, "Recent development of two-dimensional transition metal dichalcogenides and their applications," *Biochem. Pharmacol.*, vol. 20, no. 3, pp. 116–130, 2017.

[9] W. S. Yun, S. W. Han, S. C. Hong, I. G. Kim, and J. D. Lee, "Thickness and strain effects on electronic structures of transition metal dichalcogenides : 2H-MX_2 semiconductors (M = Mo , W ; X = S , Se , Te)," *Phys. Rev.,* vol. 85, pp. 1–5, 2012.

[10] X. Li and H. Zhu, "Two-dimensional MoS_2 : Properties, preparation, and applications," *J. Mater.*, vol. 1, no. 1, pp. 33–44, 2015.

[11] K. F. Mak, C. Lee, J. Hone, J. Shan, and T. F. Heinz, "Atomically thin MoS_2 : A

© University of Pretoria

new direct-gap semiconductor," *PRL*, vol. 105, pp. 2–5, 2010.

[12] M. Ikram, L. Liu, Y. Liu, L. Ma, H. Lv, M. Ullah, L. He, H. Wu, R. Wang and K. Shi "Fabrication and characterization of a high-surface area MoS_2@WS_2 heterojunction for the ultra- sensitive NO_2 detection at room temperature" *J. Mater. Chem A,* vol. 7, no. 2, pp. 14602–14612, 2019.

[13] S. Shao, L. Che, Y. Chen, M. Lai, S. Huang, and R. Koehn, "A novel RGO-MoS_2-CdS nanocomposite film for application in the ultrasensitive NO_2 detection," *J. Alloys Compd,* 2018.

[14] G. Eda, H. Yamaguchi, D. Voiry, T. Fujita, M. Chen, and M. Chhowalla, "Photoluminescence from chemically exfoliated MoS_2," *Nano Lett.* 2011.

[15] S. Yeo, D. K. Nandib, R. Rahulb, T. H. Kimb, B. Shongc, Y. Jangd, J. Baed, J. W. Hane, S. Kimb, H. Kim "Low-temperature direct synthesis of high quality WS_2 thin films by plasma-enhanced atomic layer deposition for energy related applications," *Appl. Surf. Sci.*, vol. 459, , pp. 596–605, 2018.

[16] H Li, Z. Yin, Q. He, H. Li, X. Huang, G. Lu, D. W. H. Fam, A. L. Y. Tok, Q. Zhang and Hua Zhang "Fabrication of single and multilayer MoS_2 film-based field-effect transistors for sensing NO at room temperature," *small*, vol. 8, pp 63–67, 2012.

[17] Q. Tang and D. Jiang, "Stabilization and band-gap tuning of the 1T-MoS_2 monolayer by covalent functionalization," *Chem. Mater*., vol. 27, pp 3743−3748, 2015.

[18] Y. Yin, J. Han, Y. Zhang, X. Zhang, P. Xu, Q. Yuan, L. Samad, X. Wang, Y. Wang, Z. Zhang, P. Zhang, X. Cao, B. Song and S. Jin., "Contributions of phase, sulfur vacancies, and edges to the hydrogen evolution reaction catalytic activity of porous molybdenum disulfide nanosheets," *J. Am. Chem*, 138, vol. 2, pp 7965−7972, 2016.

[19] J. Xia J, J Wang, D. Chao, Z Chen, Z Liu, J. Kuo, J. Yan and Z. X. Shen., "Phase evolution of lithium intercalation dynamics in 2H-MoS_2," *Nanoscale.*, vol. 9, pp. 7533–7540, 2017.

[20] K. Wu, H. Ma, Y. Gao, W. Hu and J. Yang ., "two-dimensional tellurene and

© University of Pretoria

transition metal," *J. Mater. Chem*, vol. 7, 7430 pp. 7430–7436, 2019.

[21] Y. Han, J. Wang, H. Wan, S. Wang, and H. Hu, "Nano materials science solution processable transition metal dichalcogenides-based hybrids for photodetection," *Nano Mater. Sci.*, pp. 1–11, 2019.

[22] M. M. Bernal and D. Milano, "Two-dimensional nanomaterials via liquid-phase exfoliation: synthesis, properties and applications ," *Carb. Nano.* pp. 159–185.

[23] S. A. Han, R. Bhatia, and S. Kim, "Synthesis , properties and potential applications of two-dimensional transition metal dichalcogenides," *Nano Converg.,* vol. 2 , 2015.

[24] A. Gupta, V. Arunachalam, and S. Vasudevan, "Liquid-phase exfoliation of MoS_2 nanosheets: The critical role of trace water," *J. Phys. Chem. Lett*, vol. 7, pp 4884−4890, 2016.

[25] C. Backes, D. Hanlon, B. M. Szydlowska, A. Harvey, R. J. Smith, T. M. Higgins, J. N. Coleman, "Preparation of liquid-exfoliated transition metal dichalcogenide nanosheets with controlled size and thickness : A state of the art protocol," *J. Vis. Exp.*, vol. 118, pp. 10–13, 2016.

[26] J. R. Brent, N. Savjani, and P. O. Brien, "Progress in materials science synthetic approaches to two-dimensional transition metal dichalcogenide nanosheets," *Prog. Mater. Sci.*, vol. 89, pp. 411–478, 2017.

[27] S. Ippolito and P. Samorı, "Tailoring the physicochemical properties of solution-processed transition metal dichalcogenides via molecular approaches," *Chem. Commun*., vol. 55, pp. 8900–8914, 2019.

[28] C. Zhang, D. Hu, J. Xu, M. Ma, H. Xing, K. Yao, J. Ji, and Z. Xu "Polyphenol-assisted exfoliation of transition metal dichalcogenides into nanosheets as photothermal nanocarriers for enhanced antibiofilm activity," *ACS Nano*, vol. 12, pp. 12347–12356, 2018.

[29] V. Forsberg, R. Zhang, J. Bäckström, and C. Dahlström, "Exfoliated MoS_2 in water without additives," *PLOS One*, pp. 1–12, 2016.

[30] V. Nicolosi, M. Chhowalla, M. G. Kanatzidis, M. S. Strano, and J. N. Coleman, "Liquid exfoliation of layered materials liquid exfoliation of layered materials,"

© University of Pretoria

vol. 340, no. June, pp. 72–75, 2013.

[31] J. Á. Silva-guillén, P. San-jose, and R. Roldán, "Electronic band structure of transition metal dichalcogenides from Ab Initio and Slater – Koster tight-binding model," *Appl. Sci.*, vol. 6, no. 284, 2016.

[32] J. Kopaczek, M. Polak, P. Scharoch, and B. Chen, "Direct optical transitions at K- and H-point of Brillouin zone in bulk MoS_2 , Direct optical transitions at K- and H-point of Brillouin zone in bulk MoS_2 , $MoSe_2$, WS_2 ," J. Appl. Phys., vol. 119, 2016.

[33] A. Splendiani, L. Sun, Y. Zhang, T. Li, J. Kim, Chi-Yung Chim, G. Galli and F. Wang "Emerging photoluminescence in monolayer MoS_2 " *Nano Lett.*, vol. 10, pp. 1271–1275, 2010.

[34] A. Molina-sánchez, K. Hummer, and L. Wirtz, "Vibrational and optical properties of MoS_2 : From monolayer to bulk," *Surf. Sci. Rep.*, vol. 70, no. 4, pp. 554–586, 2015.

[35] M. Kang, B. Kim, S. H. Ryu, S. W. Jung, and J. Kim, "Universal mechanism of bandgap engineering in transition-metal dichalcogenides,"*Nano lett.,* vol. pp. 1–19, 2017.

[36] S. J. Zelewski and R. Kudrawiec, "Photoacoustic and modulated reflectance studies of indirect and direct band gap in van der Waals crystals," *Sci. Rep.*, no. November, pp. 1–11, 2017.

[37] M. Laskar, D. N. Nath, L. Ma, E. Lee, C. H. Lee, T. Kent, Z. Yang, R. Mishra, M. A. Roldan, J. Idrobo, S. T. Pantelides, S. J. Pennycook, R. Myers, Y. Wu and S. Rajan., "p-type doping in CVD grown MoS 2 using Nb," *Appl. Phys. Lett.,* pp. 1–12, 2014.

[38] Y. Fu, Mi. Long, A. Gao, Y. Wang, C. Pan, X. Liu, J. Zeng, K. Xu, L. Zhang, E. Liu, W. Hu, X. Wang & F. Miao., "Intrinsic p-type W-based transition metal dichalcogenide by substitutional Ta-doping," *Appl. Phys. Lett.*, vol. 111, no. 4, 2017.

[39] J. Gao*,* Y. D. Kim, L. Liang, J. C. Idrobo, P. Chow, J. Tan, B. Li, L. Li, B. G. Sumpter, T. Lu, V. Meunier, J. Hone, and N. Koratkar, "Transition-metal

© University of Pretoria

substitution doping in synthetic atomically thin semiconductors," *Adv. Mater*. vol. 28, pp. 9735–9743, 2016.

[40] S. W. Glunz, S. Rein, J. Knobloch, W. Wettling, and T. Abe, "Comparison of boron- and gallium-doped p-type Czochralski silicon for photovoltaic application", *Prog. Photovolt: Res. Appl*, vol. 7, pp. 463–469, 1999.

[41] Y. Zhao, B. Liu, Z. Yu, D. Cao, and M. Cai, "Tuning charge carrier types , superior mobility and absorption in lead-free perovskite $CH_3NH_3GeI_3$: theoretical study electrochimica acta tuning charge carrier types , superior mobility and absorption in lead-free perovskite $CH_3NH_3GeI_3$: Theoretical study," *Electrochim. Acta*, vol. 247, no. July, pp. 891–898, 2017.

[42] K. Zhang, S. Feng, J. Wang, A. Azcatl, N. Lu, R. Addou, N. Wang, C. Zhou, J. O. Lerach, V. Bojan, M. J. Kim, L. Chen, R. M. Wallace, M. Terrones, J. Zhu, and J. A. Robinson "Manganese doping of monolayer MoS_2 : The substrate is critical manganese doping of monolayer MoS_2 : The substrate is critical," *Nano Lett,* pp 1-23, 2015.

[43] J. Zhua, H. Zhanga, Y. Tonga, L. Zhaoa, Y. Zhang, Y. Qiua, X. Lina, "Applied surface science first-principles investigations of metal (V, Nb, Ta) -doped monolayer MoS_2 : Structural stability , electronic properties and adsorption of gas molecules," *Appl. Surf. Sci.*, vol. 419, pp. 522–530, 2017.

[44] G. Mirabelli, M. Schmidt, B. Sheehan, K. Cherkaoui, S. Monaghan, I. Povey, M. McCarthy, A. P. Bell, R. Nagle, F. Crupi, P. K. Hurley and Ray Duffy., "Back-gated Nb-doped MoS_2 junctionless," *AIP Advances,* vol. 6, 025323, 2016.

[45] S. Qin, W. Lei, D. Liu, and Y. Chen, "In-situ and tunable nitrogen-doping of MoS_2 nanosheets," *Scientific Reports,* vol. 1, pp. 1–5, 2014.

[46] D. Kiriya, M. Tosun, P. Zhao, J. S. Kang, and A. Javey, "Air-stable surface charge transfer doping of moS_2 by benzyl viologen," *J. Am. Chem,* vol. 36, 7853−7856, 2014.

[47] J. H. Park, A. Sanne, Y. Guo, M. Amani, K. Zhang, H. C. P. Movva, J. A. Robinson, A. Javey, J. Robertson, S. K. Banerjee, A. C. Kumme "Defect

© University of Pretoria

passivation of transition metal dichalcogenides via a charge transfer van der Waals interface," *Sci. Adv*, vol. 3, pp. 1–7, 2017.

[48] W. Choi, N. Choudhary, G. H. Han, J. Park, D. Akinwande, and Y. H. Lee, "Recent development of two-dimensional transition metal dichalcogenides and their applications," *Mater. Today*, vol. 20, no. 3, pp. 116–130, 2017.

[49] J. Zhang, P. Gu, G. Long, R. Ganguly, Y. Li, N. Aratani, H. Yamadac and Qichun Zhang, "Switching charge-transfer characteristics from p- type to n-type through molecular "doping (co- crystallization)" " *Chem. Sci*, vol. 7,pp. 3851–3856, 2016.

[50] A. Phys, S. T. Le, C. A. Richter, and C. A. Hacker, "Improved contacts to p-type MoS_2 transistors by charge-transfer doping and contact engineering Improved contacts to p-type MoS_2 transistors by charge-transfer doping and contact engineering," *Appl. Phys. Lett*., vol. 115, pp 073106, 2019.

[51] S. Mouri, Y. Miyauchi, and K. Matsuda, "Tunable photoluminescence of monolayer MoS_2 via chemical doping," *Nano Lett,* vol. 13, pp 5944−5948, 2013.

[52] M. Mos, P. Rastogi, S. Kumar, S. Bhowmick, A. Agarwal, and Y. S. Chauhan, "Ab-initio study of doping versus adsorption in monolayer MoS_2," vol. 1, 2015.

[53] S. Andleeb, A. K. Singh, J. Eom, S. Andleeb, A. K. Singh, and J. Eom, "Chemical doping of MoS_2 multilayer by p-toluene sulfonic acid chemical doping of MoS_2 multilayer by p-toluene sulfonic acid," *Sci. Technol. Adv. Mater.*, vol. 16, no. 3, p. 35009, 2015.

[54] C. H. Lianga , S. Y. Hub , Y. H. Chana , S. K. Wanga , K. K. Tionga , Y. S. Huang "Synthesis and characterization of flower-like Au-doped MoS_2 C. H. Liang," ECS Transactions., vol. 25, no. 9, pp. 183–191, 2009.

[55] Y. Lin, D. O. Dumcenco, H. Komsa, Y. Niimi, and V. Arkady, "Properties of individual dopant atoms in single-layer MoS_2 : atomic structure, migration and enhanced reactivity." *Adv. Mater*., vol. 26, no. 18, pp. 2857-2861 2014.

[56] J. Wang, Q. Zhou, Z. Lu, Y. Gui, and W. Zeng, "Physica E : Low-dimensional systems and nanostructures adsorption of H_2O molecule on TM (Au, Ag)

© University of Pretoria

doped-MoS_2 monolayer : A first- principles study," *Physica E Low Dimens. Syst. Nanostruct.*, vol. 113, no. April, pp. 72–78, 2019.

[57] L. Zeng, Y. Liu, S. Lin, W. Qarony, L. Tao, Y. Chai, X. Zhang, S. P. Lau, H. Tsang "Solar energy materials and solar cells high photoelectrochemical activity and stability of Au-WS_2 / silicon heterojunction photocathode," *Energ. Mat. Sol. C.,* vol. 174, pp. 2017–2019, 2018.

[58] H. Li, D. Lee, D. Qu, X. Liu, J. Ryu, A. Seabaugh and W. J. Yoo, "Ultimate thin vertical p–n junction composed of two-dimensional layered molybdenum disulfide," *Nat. Commun.*, pp. 1–9, 2015.

[59] X. Gu , W. Cui , H. Li , Z. Wu , Z. Zeng , S. Lee , H. Zhang and B. Sun "A solution-processed hole extraction layer made from ultrathin MoS_2 nanosheets for efficient organic solar cells," *Adv. Energy Mater.*, vol. 3, pp. 1262–1268, 2013.

[60] M. Tsai, S. Su, J. Chang, D. Tsai, C. Chen, C. Wu, L. Li, L. Chen and H. He., "Monolayer MoS_2 heterojunction solar," *ACS. nano.*, vol. 8, pp. 8317–8322, 2014.

[61] H. Xu,L. Xin, L. Liu, D. Pang, Y. Jiao, Ridong Cong and W. Yu., "Large area MoS_2 / Si heterojunction-based solar cell through sol-gel method," *Mater. Lett.*, vol. 238, pp. 13–16, 2019.

[62] Y. Lin, Y.Wang, H. An, B. Qi, J. Wang, L. Wang, J.Shi, L. Mei and H. Wang "Peptide-based autophagic gene and cisplatin co-delivery systems enable improved chemotherapy resistance," *Nano Lett.*, vol. 19, pp. 2968–2978, 2019.

[63] A. Thilagam, "Transition-metal dichalcogenide heterostructure solar cells: A numerical study," J. Math Chem., vol. 55, pp. 50-64, 2017.

[64] https://en.wikipedia.org/wiki/Heterojunction#/media/File:Heterojunction_types.png, December 03, 2019.

[65] A. G. Dandridge, S. W. Dunworth, and J. Thomas, "15 Phthalocyanine pigments and dyes," *colour chemistry.,* pp. 231–240, 1971

[66] P. A. Barret, R. P. Linstead and G. A. P. Tuey "Phthalocyanines and related compounds. Part X V. Tetrabenx- triaxaporphin: its preparation from

© University of Pretoria

phthalonitrile and a proof of its structure.," *J. Chem. Soc.*, pp. 1809-1820 1939.

[67] R. P. Linstead, " Phthalocyanines. Part I. A new type of synthetic coburing matters" *J. Chem. Soc.,* vol. 212, pp 1016-1017, 1934.

[68] W. Dieter , G. Schnurpfeil, S. G. Makarov, A. Kazarin, and O. N. Suvorovab "Practical applications of phthalocyanines – from dyes and pigments to materials for optical , electronic and photo-electronic devices," *Macroheterocycles,* vol. 5, no. 3, pp. 191–202, 2012.

[69] C. Murray, N. Dozova, J. G. Mccaffrey, and S. Fitzgerald, "Infra-red and Raman spectroscopy of free-base and zinc phthalocyanines isolated in matrices," *Phys. Chem. Chem. Phys*, vol. 12, pp. 10406–10422, 2010.

[70] S. Mori and N. Shibata, "Synthesis and application of trifluoroethoxy-substituted phthalocyanines and subphthalocyanines," *J. Org. Chem,* Vol. 13, pp. 2273–2296, 2017.

[71] X. Wang, L. Zhi, and K. Mu, "Transparent , conductive graphene electrodes for dye-sensitized solar cells," *Nano Lett*, vol. 8, pp 323-327, 2008.

[72] R. Li, X. Zhang, P. Zhu, D. K. P. Ng, N. Kobayashi, and J. Jiang, "Electron-donating or -withdrawing nature of substituents revealed by the electrochemistry of metal-Free phthalocyanines," *Inorg. Chem.* vol. 45, no. 5, pp. 1636–1637, 2006.

[73] R. Shankar and N. K. Jha, "Synthesis of soluble phthalocyanines and study of their aggregation behaviour in solution," *Indian J. Chem.,* vol. 32, pp. 1029–1033, 1993.

[74] Y. Li, Bin Wang, Z. Yu, X. Zhou, D. Kang, Y. Wu, Z. Chen, C. Hea and X. Zhou "The effects of central metals on ammonia sensing of metallophthalocyanines covalently bonded to graphene oxide hybrids," *RSC advances*, vol. 7, pp. 34215–34225, 2017.

[75] M. N. Yarasir, M. Kandaz, O. Güney, and B. Salih, "Synthesis and photophysical properties of metallophthalocyanines substituted with a benzofuran based fluoroprobe," *Spectrochim. Acta Part A Mol. Biomol.*

© University of Pretoria

Spectrosc., vol. 93, pp. 379–383, 2012.

[76] N. A. Kuznetsova and O. L. Kaliya, “Heterogenized metallophthalocyanines for photodynamic microorganism inactivation : an overview of our experience heterogenized metallophthalocyanines for photodynamic microorganism inactivation : an overview”. *Macroheterocycles*, vol. 8, pp 8-19, 2015.

[77] A. Paja, P. Rybinski, G. Janowska, A. Kucharska-Jastrzabek “The thermal properties and the flammability of pigmented elastomeric materials,” *J. Therm. Anal. Calorim.*, vol. 117, pp. 789–798, 2014.

[78] I. Kim, H. M. Haverinen, Z. Wang, S. Madakuni, Y. Kim, J. Li and G. E. Jabbour., “Efficient organic solar cells based on planar metallophthalocyanines,” *Chem. Mater*, vol. 85, no. 2, pp. 4256–4260, 2016.

[79] P. Y. Stakhira, I. I. Grygorchaka, V. V. Cherpaka, F. O. Ivastchyshyna, D. Y. Volynyuka, G. Luka, M. Godlewski, E. Guziewicz, G. L. Pakhomov, Z. Y. Hotra “Long time stability of ITO / NiPc / ZnO / Al devices with ZnO buffer layer formed by atomic layer deposition technique – impedance spectroscopy analysis,” *Mater. Sci. Eng. B*, vol. 172, no. 3, pp. 272–275, 2010.

[80] A. A. M. Farag and A. A. A. Darwish, “Photovoltaic properties of NiPc / p-Si (organic / inorganic) heterojunctions,” *Org. Electron.,* vol. 6, pp. 129–136, 2005.

[81] J. Pak, M. Min, K. Cho, D. Lien, G. H. Ahn, J. D. Yoo, S. Chung, A. Javey, and T. Lee, “Improved photoswitching response times of MoS_2 field-effect transistors by stacking p -type copper phthalocyanine layer,” *Appl. Phys. Lett.,* vol. 109, pp. 3–6, 2016.

© University of Pretoria

Chapter 3: Materials and methods

3.1 Experimental section

3.1.1 Materials

Acetone, dimethylformamide (DMF), isopropyl alcohol and N-methyl-2-pyrrolidone (NMP) were all purchased from Radchem (Pty) LTD. Copper phthalocyanine (CuPc), flourine doped tin oxide (FTO), gold (III) chloride ($AuCl_3$), iron phthalocyanine (FePc), manganese phthalocyanine (MnPc) and nickel phthalocyanine (NiPc) were purchased from Sigma-Aldrich. Molybdenum disulphide (MoS_2) and tungsten disulphide (WS_2) were purchased from Protea laboratory solution (Pty) LTD.

3.1.2 Instrumentation

Synthesis of TMD nanosheets was carried out in an ultrasonic bath from Labotech (using model 704). Spin coating was carried out using a Laurell technology spin coater model WS-650MZ-23NPPB. Samples were centrifuged using a thermo scientific Labofuge 700 centrifuge.

X-ray diffraction (XRD)

X-ray diffraction (XRD) analysis was conducted using a Bruker D2 PHASER-e diffractometer using Cu-Kα radiation (0.15418 nm).

XRD is used to identify the phase of a material, additionally, it can provide information about orientation, grain size and crystallographic structure. XRD analysis involves constructive interference of monochromatic X-rays with a crystalline sample. This interference is accompanied by a diffraction of the X-ray beam into the detector. Constructive interference can only occur when conditions for Bragg's law are satisfied ($n\lambda = 2d\sin\theta$). Bragg's law relates the wavelength of electromagnetic radiation with the angle of diffraction. Each sample has a unique XRD pattern which is provided by unique XRD fingerprints of the crystals present in the sample. These fingerprints make it easy to identify the crystals.

© University of Pretoria

Raman spectroscopy

Raman spectroscopy measurements were recorded on a WiTec alpha300 RAS+ Confocal Raman microscope with 532 nm excitation laser at 5 mW.

Raman spectroscopy is a technique which gives information about molecular vibrations. It also provides information about rotational and other low frequency modes in a molecule. This spectroscopic technique helps to identify molecules by providing their structural fingerprints. The system involves the use of a monochromatic light such as a laser which interacts with molecular vibrations causing energy of the laser to be shifted up or down by Raman scattering. These shifts give information about vibrational modes in the sample.

Scanning electron microscopy (SEM)

Scanning electron microscopy (SEM) was carried out on a crossbeam 540 FEG SEM microscope from Zeiss.

SEM is a technique that gives images of a sample by scanning its surface with a focused high energy electron beam. Interaction of these high energy electrons with the surface of the sample gives out a variety of signals that contain information about topography, composition and the external morphology of the sample.

The crossbeam 540 FEG was coupled with energy dispersive X-ray spectroscopy which was used for the determination of elemental composition of the samples. Commonly referred to as EDS, energy-dispersive X-ray spectroscopy is a technique used for the chemical characterisation of samples. This technique involves the interaction of a sample with a beam of electrons followed by the detection of X-rays emitted by the sample. Each element has a unique atomic structure, this unique structure generates corresponding sets of peaks on the electromagnetic emission spectrum. The detailed mechanism of this technique includes the use of a high-energy beam of charged particles. This high-energy beam is focused on a sample which has elements with different atomic structures. The beam causes electrons in the innermost energy level to be ejected, leaving a hole behind. Consequently, an electron in a higher energy level falls to the hole, releasing energy in that process. This energy is released in form of X-rays. The instrument then measures the number and energy of X-rays

© University of Pretoria

emitted due to the interaction of the high energy beam and the sample. The energy of the X-rays emitted is a characteristic of the difference between two energy levels and the structure of the emitting element. As such elemental analysis can be done.

Ultraviolet-visible (UV-vis) spectroscopy

UV-vis absorption measurements were taken on a CARY 100 BIO UV-Vis spectrophotometer.

This characterisation technique involves absorption of light by a molecule in the UV-vis region of the electromagnetic spectrum. Absorption of this light results in excitation of the molecule from the highest occupied molecular orbital (HOMO) to the lowest unoccupied molecular orbital (LUMO) (i.e. valence band to conduction band). The energy of the molecule of light absorbed equals to the energy between the HOMO and LUMO of the material.

Electrochemical studies

Current-voltage (I–V) measurements were conducted on a B2900 solar management unit (SMU). Illuminated I–V measurement were performed using a Model 91150V solar simulator with solar output conditions of 1000 W/m^2 at 25 °C and AM 1.0 G reference spectral filtering, which is the air mass coefficient used universally for measuring performance of a solar cell.

3.2 Synthesis

3.2.1 Synthesis of MoS_2 nanosheets

Synthesis of MoS_2 was done following a previously reported procedure [1]. The liquid-based exfoliation method was followed to obtain a large quantity of MoS_2. Briefly, 0.5 g of MoS_2 powder was added into 10 mL N-methyl-2-pyrrolidone (NMP) which was the exfoliating agent. The concentration of the resulting mixture was 5 mg.mL^{-1}. The mixture was then sonicated for 6 h at 5°C. The mixture was left to settle for 72 hours. The upper three quarters of the mixture was decanted into a centrifuge tube and

© University of Pretoria

centrifuged at 3000 rpm for 30 minutes and the supernatant was collected and deposited as a thin film on a glass substrate for characterisation.

3.2.2 Synthesis of WS_2 nanosheets

Synthesis of WS_2 was done following a modification of a previously reported procedure [2]. The liquid-based exfoliation method was followed to obtain a large quantity of WS_2. Briefly, 0.1 g of WS_2 powder was added into 10 mL N'N'-dimethylformamide which was the exfoliating agent. The resulting concentration was 10 mg.mL^{-1}. This led to a black mixture. The mixture was then sonicated for 6 h while maintaining a temperature of 5 °C. The mixture was left to settle for 72 hours. The upper three quarters of the mixture was decanted into a centrifuge tube and was centrifuged at 1500 rpm for 45 minutes to remove unexfoliated material. The supernatant was collected and deposited on a glass substrate for characterisation.

3.2.3 Doping of MoS_2 and WS_2 with gold

Doping was done following a procedure previously reported [3]. An aqueous gold solution (20 mM) was prepared by dissolving 0.3 g of $AuCl_3$ in distilled water. On TMD coated glass substrate, 10 μL of the gold solution was spin coated at 2500 rpm for 1 minute. The resulting sample was annealed at 100 °C for 10 minutes to obtain the Au doped TMDs.

3.3 Solar cell fabrication

FTO-coated glass substrates were cleaned thoroughly by sonication in 2-propanol, then in acetone, and lastly in distilled water for 10 minutes in each solvent. Subsequently, a TMD dispersed in an organic solvent was spin coated on FTO at 1500 rpm (MoS_2) or 2000 rpm (WS_2). Thereafter, aqueous $AuCl_3$ (20 mM) was spin coated on top of the TMD layer. The FTO substrate was annealed at 100 °C for 10 minutes. The sample was placed in a physical vapour deposition bell jar where a layer of a metallophthalocyanine was deposited. The thickness of the MPc film was maintained

© University of Pretoria

at 200 nm. Another TMD layer was deposited by spin coating on top of the MPc film. The resulting sample was annealed at 210 °C for 60 minutes. A gold contact of thickness 100 nm was deposited using physical vapour deposition.

Solar cells fabricated in this study are listed below:

1. Glass/FTO/Au-MoS_2/CuPc/MoS_2/Au
2. Glass/FTO/Au-WS_2/CuPc/WS_2/Au
3. Glass/FTO/Au-MoS_2/FePc/MoS_2/Au
4. Glass/FTO/Au-WS_2/FePc/WS_2/Au
5. Glass/FTO/Au-MoS_2/MnPc/MoS_2/Au
6. Glass/FTO/Au-WS_2/MnPc/WS_2/Au
7. Glass/FTO/Au-MoS_2/NiPc/MoS_2/Au
8. Glass/FTO/Au-WS_2/NiPc/WS_2/Au

© University of Pretoria

3.4 References

[1] U. Dasgupta, S. Chatterjee, and A. J. Pal, "Thin-film formation of 2D MoS_2 and its application as a hole-transport layer in planar perovskite solar cells Solar Energy Materials and Solar Cells Thin-film formation of 2D MoS_2 and its application as a hole-transport layer in planar perovskite solar cells," *Sol. Energ. Mat. Sol C.*, vol. 172, pp 353–360, 2017.

[2] G. Han, Y. Liu, W. Hu, B. Dong, X. Li, and Y. Chai, "WS_2 nanosheets based on liquid exfoliation as effective electrocatalysts for hydrogen evolution reaction," *Mater. Chem. Phys.*, vol. 167, pp. 271–277, 2015.

[3] H. Li, D. Lee, D. Qu, X. Liu, J. Ryu, A. Seabaugh and W. J. Yoo "Two-dimensional layered molybdenum disulfide," *Nat. Commun.*, vol. 6, pp. 1–9, 2015.

© University of Pretoria

Chapter 4: Results and discussion

4.1. Characterisation of MoS_2 and WS_2 nanosheets

4.1.1 XRD

Bulk TMDs underwent XRD characterisation before exfoliation and the results were recorded. After exfoliation, the materials were spin coated onto a microscope glass substrate, annealed and taken for XRD characterisation. Figure 4.1a shows the XRD pattern of the bulk MoS_2 which was indexed according to JCPDF card number 06-0097 [1]. This XRD spectrum confirms the crystal structure of MoS_2. The XRD pattern shows a diffracted peak at 2θ= 14.4° (002) and other peaks with low intensities at 2θ= 29° (004), 2θ= 33° (001), 2θ= 34° (101), 2θ= 39.56° (103) and 2θ=49.8° (105).

After exfoliation, the sample was characterised and the resulting XRD pattern is shown on Figure 4.1b. This XRD diffractogram did not have all the peaks exhibited by the diffractogram of the bulk material. Only one peak was maintained. This peak is at 2θ=14.4° and is indexed as the (002) peak. This maintained peak has a lower intensity when compared the (002) peak for the bulk material and this was also reported elsewhere [2]. The (002) peak provides a useful information for determining if the TMD material is bulk or if it is mono- or few layered. Maintaining the peak with others disappearing shows that exfoliation has taken place [3]. A decrease in intensity of the peak suggests that exfoliation has indeed taken place and single layers are dominating the sample.

© University of Pretoria

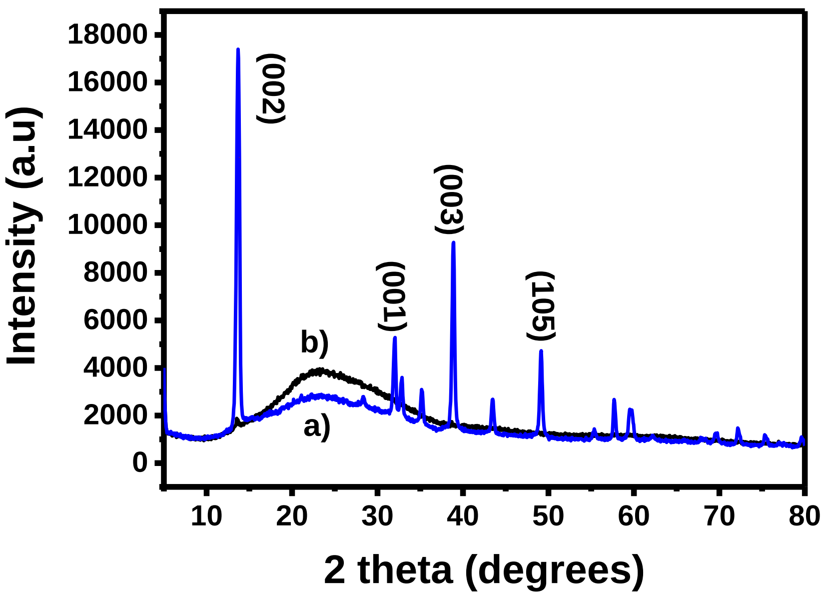

Figure 4.1: XRD spectra for (a) bulk and (b) exfoliated MoS_2.

As done for MoS_2, bulk WS_2 material underwent XRD characterisation before and after exfoliation. Figure 4.2a shows the XRD diffractogram of bulk WS_2 material. Indexing of the diffractogram of WS_2 was done using the JCPDS file no. 08-0237 and it confirmed the crystalline structure of WS_2. The diffractogram exhibited several peaks at 2 theta values 14.4°, 29°,33°,34°,39.8° and 44.9° indexed (002), (004), (001), (101), (103) and (006), respectively. The bulk material underwent exfoliation. The resulting sample was spin coated on glass and taken for XRD characterisation. Figure 4.2b shows the diffractogram for WS_2 after exfoliation has taken place and Figure 4.2c shows the XRD spectrum of the bare glass substrate that the exfoliated WS_2 was deposited on. The XRD pattern for WS_2 after exfoliation does not have all the peaks exhibited by its bulk counterpart. This XRD pattern shows that out of all the peaks, only one peak was maintained when moving from bulk to mono- or few layered WS_2. The maintained peak is the (002) peak found at $2\theta = 14.4^{o}$. This peak is known to be sensitive to layering of the material. Since only the (002) peak is maintained, this suggest that exfoliation has successfully taken place. A decrease in intensity of the (002) peak implies that the sample is highly exfoliated and monolayers are dominating the sample. The diffractogram of exfoliated WS_2 showed the presence of foreign peaks. The microscope glass slide which was used as the glass substrate was taken

© University of Pretoria

for XRD characterisation and its diffraction pattern (Figure 4.2c) showed that the foreign peaks observed for exfoliated WS_2 align with those of the of the glass substrate hence they are from the glass substrate [4].

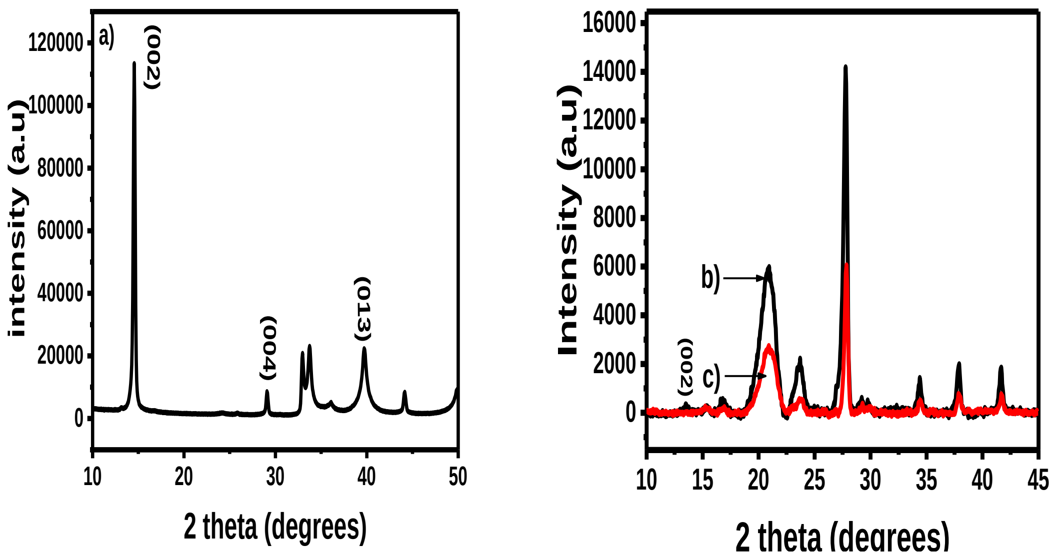

Figure 4.2: XRD spectra for (a) bulk WS_2, (b) exfoliated WS_2 and (c) the bare glass substrate.

4.1.2 Raman spectroscopy

The Raman fingerprint for MoS_2 is evidenced by vibrations at ~380 cm^{-1} and ~410 cm^{-1}. These vibrations are known as the E^1_{2g} and A_{1g} peak, respectively. The E^1_{2g} peak gives information about the in-plane opposite vibrations of sulfur and molybdenum atoms while the A_{1g} gives information about the out-of-phase vibrations of the sulfur atoms. Raman spectroscopy can further be used to confirm if exfoliation has indeed taken place [5]. This confirmation can be done by comparing the Raman spectra of the exfoliated and the bulk MoS_2 material. When moving from bulk to few layers of MoS_2 sheets, the distance between the two Raman peaks, E^1_{2g} and A_{1g}, reduces indicating exfoliation has taken place [5].

Figure 4.3a shows the Raman spectrum for MoS_2 before it was subjected to exfoliation. As expected from the Raman fingerprint of MoS_2, the bulk material

© University of Pretoria

exhibited the E^1_{2g} and A_{1g} peaks at 378 cm^{-1} and 408 cm^{-1}, respectively. The distance between the two peaks was found to be 30 cm^{-1}.

Figure 4.3b shows the Raman spectrum for exfoliated MoS_2. The spectrum contains two peaks and they are found at Raman shifts 393 and 409 cm^{-1}. The distance between the two peaks was calculated to be 16 cm^{-1}. This was a reduction from 30 cm^{-1} for bulk material. As such, it can be concluded that exfoliation has indeed taken place.

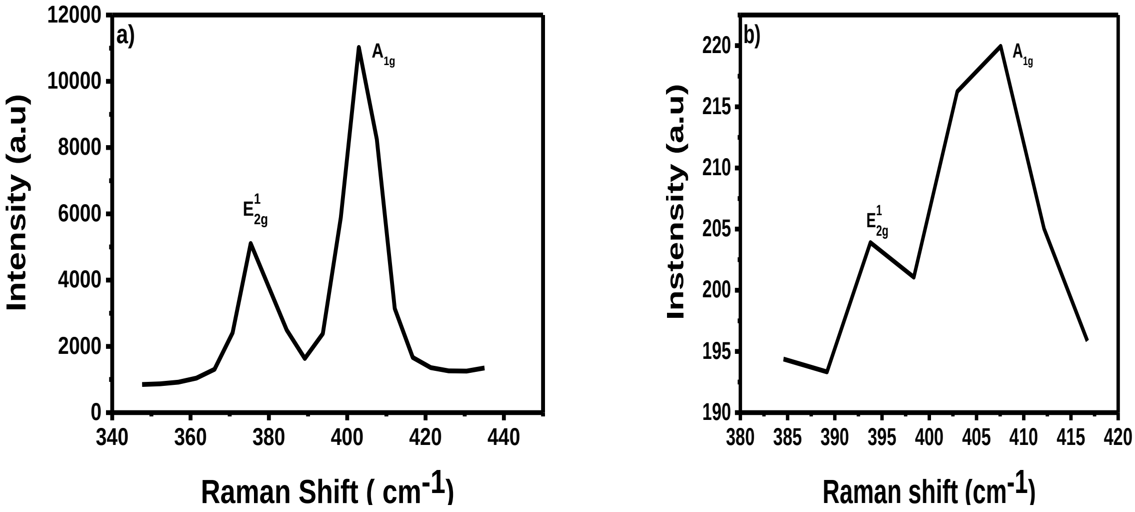

Figure 4.3: Raman spectra for (a) bulk MoS_2 and (b) exfoliated MoS_2.

Similarly to MoS_2, the Raman spectrum for WS_2 exhibits the two typical peaks. However, the E^1_{2g} peak for these two different materials vibrate at different positions on the spectrum. A typical Raman spectrum for WS_2 has the E^1_{2g} peak at ~350 cm^{-1} and the A_{1g} peak vibrates at ~410 cm^{-1}. As in the case for MoS_2, the E^1_{2g} peak provides information about the in-plane opposite vibration of sulfur and tungsten atoms while on the other hand, A_{1g} provides information about the out of phase vibrations of the sulfur atoms.

Figure 4.4a shows the Raman spectrum for bulk WS_2. The E^1_{2g} peak was found to vibrate at 350 cm^{-1} while the A_{1g} was found to vibrate at 411 cm^{-1}. The distance between the two peaks was calculated to be 61 cm^{-1}. Figure 4.4b shows the Raman spectrum for exfoliated WS_2. On the spectrum, the E^1_{2g} and the A_{1g} peaks vibrate at 355 cm^{-1} and 408 cm^{-1}, respectively. The distance between the two peaks was found

© University of Pretoria

to be 53 cm^{-1}. This is a reduction from 61 cm^{-1} reported for bulk material confirming that exfoliation has successfully taken place [6-7].

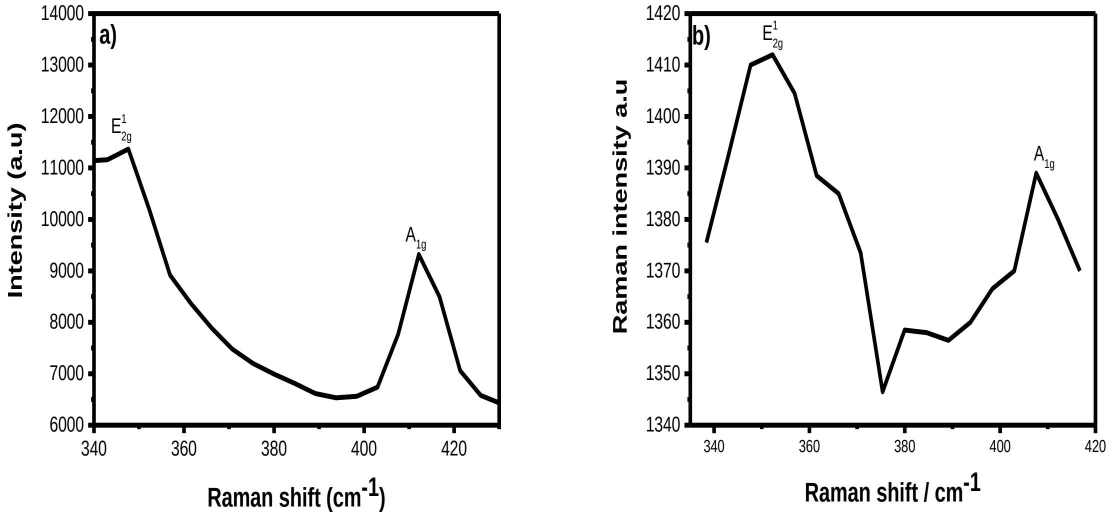

Figure 4.4: Raman spectra for (a) bulk WS_2 and (b) exfoliated WS_2.

4.1.3 SEM

The TMDs were taken for morphology characterisation using scanning electron microscopy (SEM). The aim was to confirm if indeed going from bulk to exfoliated TMDs, the formation of few layered nanosheets can be observed. Figure 4.5a shows the SEM micrograph for bulk MoS_2. The morphology observed is that of nanoflakes. Isolating each nanoflake, it can be observed that they are made up of several layers stacked together. These layers are held together by weak van der Waals forces which are easily overcame by exfoliation. Thereafter, the bulk MoS_2 underwent exfoliation in NMP for three hour and the sample was taken for SEM characterisation. Figure 4.5b shows the SEM micrograph for the resulting material at a higher magnification. The morphology observed was nanosheets. However, the nanosheets were still stacked together into a number of layers of different size and the layers were fewer as compared to the micrograph of the bulk material. This suggest that exfoliation has occurred. However, more time was needed for the nanosheets to be separated

© University of Pretoria

completely. The material was exfoliated further for a total of six hours. Figure 4.5c shows the micrograph for the resulting material. The micrograph shows a monolayer nanosheet morphology indicating that exfoliation has taken place completely and single layered materials were dominating the sample.

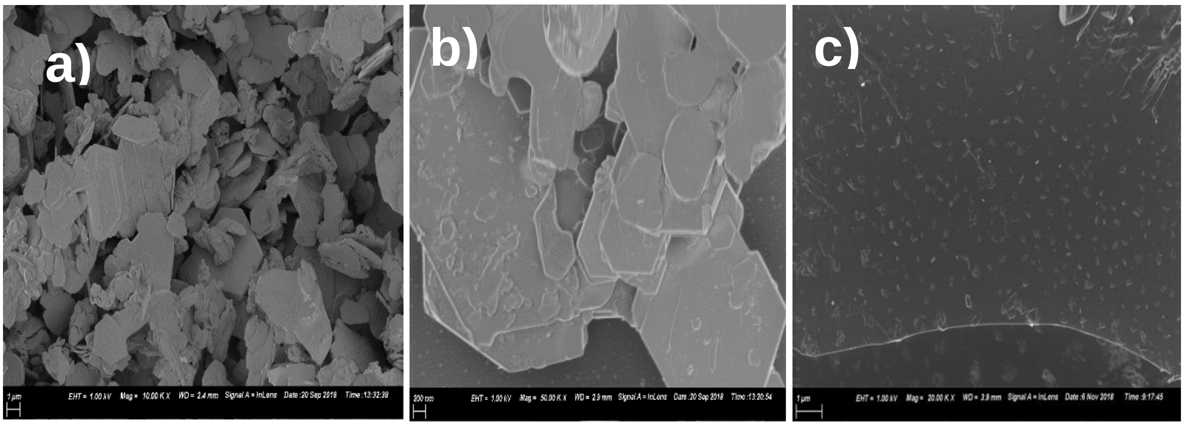

Figure 4.5: SEM micrograph of (a) bulk MoS_2 (1 μM magnification), (b) MoS_2 exfoliated for 3 hours (200 μM magnification) , (c) MoS_2 exfoliated for 6 hours (1 μM magnification).

Figure 4.6a shows the SEM micrograph for bulk WS_2. Similarly to the micrograph of bulk MoS_2, nanoflakes are observed as the morphology of bulk WS_2. Figure 4.6b shows the SEM micrograph for exfoliated WS_2. This micrograph shows that after exfoliation has taken place, a monolayer layer nanosheets are observed. The resulting nanosheet has a smooth surface. Nanosheets of this nature where also reported previously [8].

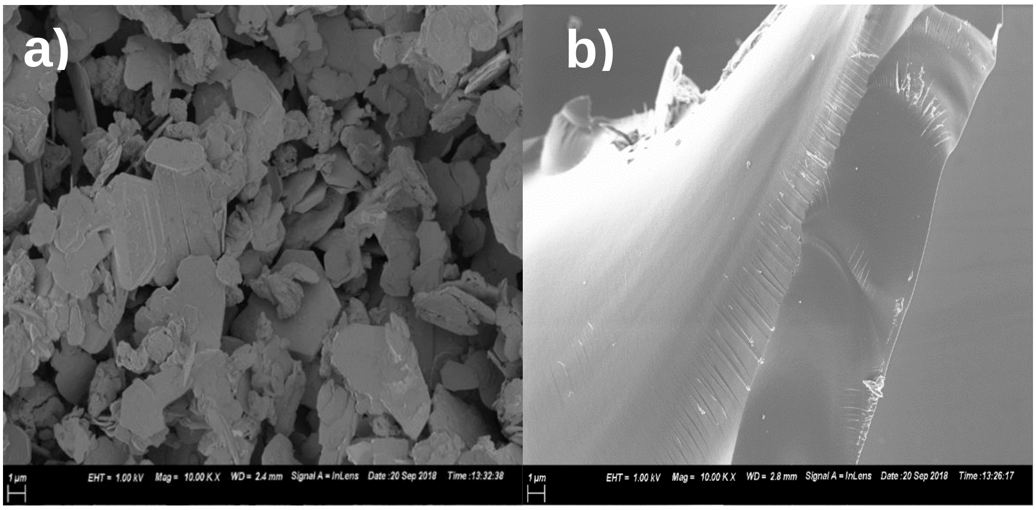

© University of Pretoria

Figure 4.6: SEM micrograph for (a) bulk WS_2 (1 μM magnification) and (b) monolayer WS_2 (1 μM magnification).

4.2 Characterisation of metallophthalocyanines

4.2.1 Raman spectroscopy

Figure 4.7a-d shows Raman spectra for all the MPc's used in this study. The spectra show that MPc's have a peak observed at ~592 cm^{-1} known as the A_{1g} peak. This peak is related to the deformation of the benzene rings. The second peak observed from all the MPc's spectra is found at ~678 cm^{-1}. This peak is called the B_{1g} and it is associated with benzene breathing. There are other several peaks for all the MPc's with lower intensities found between 800 and 1200 cm^{-1} which provide information about C-N stretching, isoindole in plane bending, C-H bending and out of plane C-H bending [9].

Other peaks are found between 1300 cm^{-1} and 1600 cm^{-1} which are useful for determination of the central metal ion. Within this range, there is a coupling of 2 Raman spectra. The two coupled Raman spectra are B_{1g} +E_g and A_{1g} + B_{2g}. The peaks observed in this range are located at the Raman shifts of ~1342, ~1468 and anywhere between 1500-1600 cm^{-1} depending on the central metal atom. The peak that is located at ~1342 cm^{-1} provides information about pyrrole stretching. This peak is called the B_{2g} peak and it gives information about stretching of bonds such as $C\alpha$ – N_β, $N\alpha$-$C\alpha$ – C_β and C – C – H [9]. The peak observed at Raman shift of ~1468 cm^{-1} provides information about the isoindole ring stretching while the peak observed at Raman shifts between 1500 and 1600 cm^{-1} is the peaks B_{1g} + A_{1g} clustered together into one vibration. Accurate assignment of these vibrations is important as both the vibrations are sensitive to the size of the metal ion at the centre of the phthalocyanine. The peak gives information about the vibrations observed on the $C\alpha$ – N_β – $C\alpha$ bridge bond. B_{1g} peak also gives information about vibrations that occur as a result of benzene stretching.

The B_{1g} + A_{1g} peak for CuPc, NiPc, FePc and MnPc are observed at 1527, 1551, 1518 and 1532, respectively.

© University of Pretoria

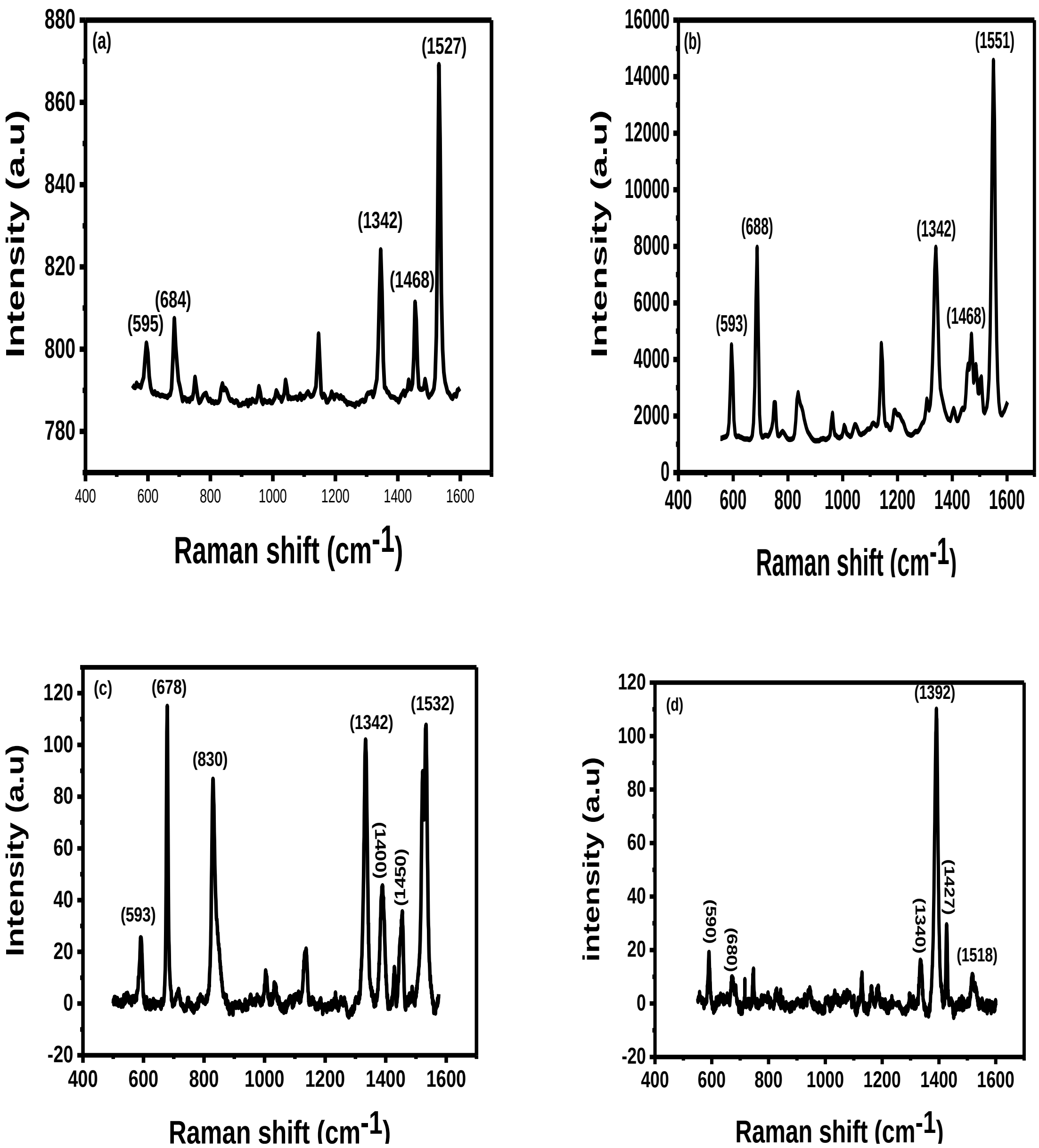

Figure 4.7: Raman spectra for (a) CuPc, (b) NiPc, (c) FePc and (d) MnPc.

4.2.2 UV-Vis spectroscopy

Metallophthalocyanines are going to be used in this study as photoactive layers for solar cell devices. For a compound or material to be used as a photoactive layer for solar cell applications, the most important characteristic required is the ability to absorb visible light from the sun. UV-vis is a useful tool for the determination of light absorption capabilities of the material. As such, it was necessary to test all the MPc's using UV-

© University of Pretoria

vis to detect if they can absorb light in the visible region of the electromagnetic spectrum.

Metallophthalocyanines were deposited by physical vapour deposition on glass substrates and the thin films were taken for UV-Vis characterisation. Figure 4.8 illustrates the UV-Vis spectrum of CuPc thin film. The UV-Vis spectra of CuPc exhibits three prominent absorption peaks. These absorption peaks are at wavelengths ~350 nm, ~620 nm and ~700 nm. The absorption peak that occurs at the wavelength ~350 nm is associated with the Soret band of the phthalocyanine ring. This Soret band is associated with π to π^* electronic transitions (b_{2u} to e_g) [10]. While, on the other hand, the absorption peaks observed at ~ 620 nm and ~700 nm are associated with the Q band of the dimer and the monomer of the CuPc molecule. The Q band occurs as a result of electronic excitation of the π electrons from the HOMO to the LUMO of the Pc ring (a_1 to e_g) [10]. From the UV-Vis spectrum of CuPc, the Q band fall within the range of visible light [11-12]. MnPc, FePc and NiPc all exhibit similar profiles (See appendix). This suggest that these materials can absorb visible light from the sun making them viable candidates for being used as photoactive layers in solar cells.

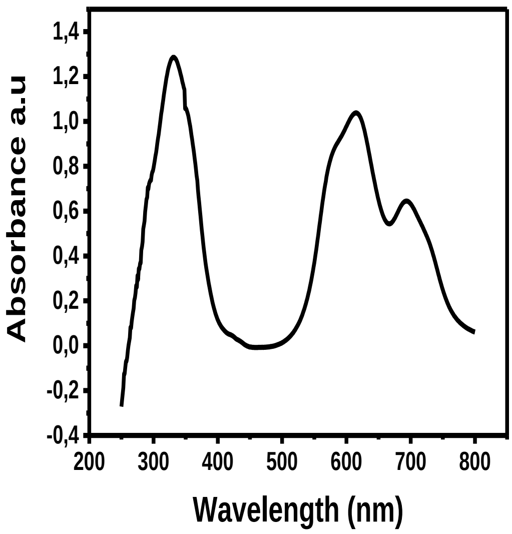

Figure 4.8: UV-Vis spectra of CuPc.

4.3 Characterisation of the MPc/TMD junctions.

The device that will be fabricated in this study will consist of these materials put against each other as different layers (TMDs and MPc's). Therefore, it is important to conduct

© University of Pretoria

a study that would provide information about the structural integrity and stability of these materials.

4.3.1 Raman spectroscopy

To confirm that the layers in the junction are not disturbed and new bonds were not formed, Raman spectroscopy was conducted on the samples. For MoS_2, the range of the Raman spectrum to be considered is 380 cm^{-1} to 420 cm^{-1} while for NiPc the the range to be considered is between 1300 and 1600 cm^{-1}. As such, the spectrum was broken down into these ranges to visualise both the materials' vibrations individually. Figure 4.9a, which is the first part of the spectrum to be isolated was the MoS_2 range. From this range, the characteristic, E^1_{2g} and A_{1g}, peaks, were observed. This shows that the material has S and Mo atoms and it further imparts on the fact that these elements are bonded together in a manner that MoS_2 atoms bond, meaning that the nanosheets were not disturbed upon coating over the NiPc film and no new bonds have formed by either the Mo or the S atoms and the old bonds of MoS_2 have not been broken as well. Shifting focus to Figure 4.9b, the spectrum range observed is of NiPc. The peaks for NiPc at this range were maintained. This shows that the NiPc material after being coated with MoS_2 remained intact and the atoms of NiPc have not formed new bonds and the old bonds of the materials have not been broken.

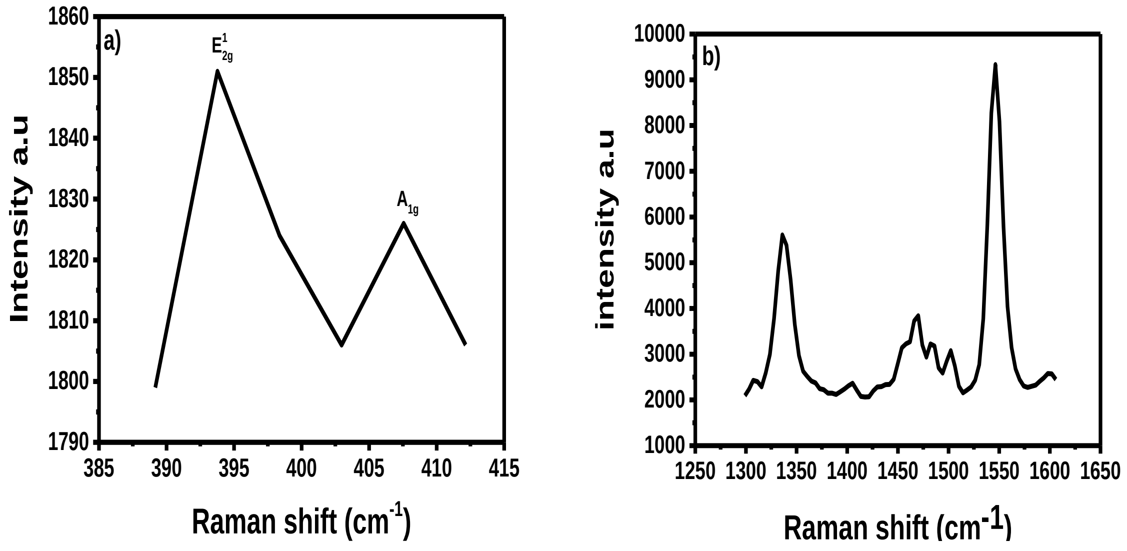

Figure 4.9: Raman spectrum for NiPc/MoS_2 bilayer separated into 2 regions, (a) 385 – 415 cm^{-1} (exfoliated MoS_2 region) and (b) 1250 – 1650 cm^{-1} (NiPc region)

© University of Pretoria

For WS_2, the range of the Raman spectrum to be considered is 350 cm^{-1} to 420 cm^{-1} while for NiPc, the range considered was between 1300 and 1600 cm^{-1}. The entire spectrum taken for the bilayer junction was broken down into these two ranges to visualise both the materials' vibration individually. Figure 4.10a, which is the first part of the spectrum to be isolated, was the WS_2 range. From this range, the characteristic peaks of WS_2, E^1_{2g} and A_g were observed. This confirms that the material has S and W atoms and it further imparts on the fact that these elements are bonded together in a manner that the atoms of WS_2 bond. This means that the nanosheets were not disturbed upon coating over the NiPc film and no new bonds have formed by either the W or the S atoms and the bonds of WS_2 have not been broken as well. Now focusing on Figure 4.10b, the spectrum range observed is of NiPc. This shows that the NiPc material after being coated by WS_2 remained intact and the atoms of NiPc have not formed new bonds and the old bonds of the materials have not been broken.

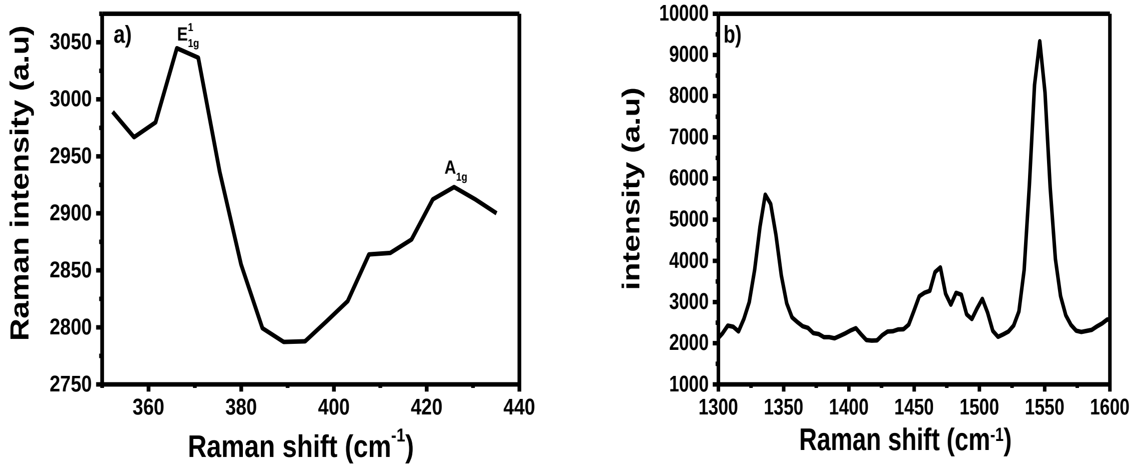

Figure 4.10: Raman spectrum for NiPc/WS_2 bilayer separated into 2 regions, (a) 350 – 440 cm^{-1} (exfoliated WS2 region) and (b) 1250 – 1650 cm^{-1} (NiPc region)

Similar results were obtained for the CuPc/TMD, MnPc/TMD and FePc/TMD composites.

© University of Pretoria

4.3.2 EDS

EDS was performed to confirm the elemental composition of all the elements in the layers. Figure 4.11a shows the EDS energy spectrum for NiPc/MoS_2 and it confirms the presence of all the elements found in these two materials which are Mo, Ni, S and N. Table 4.1 shows the percentage composition of elements found in the materials on this junction. The EDS energy spectrum for these two layers also shows other clusters of peaks which correspond to usual surface contaminants like oxygen. Other foreign peaks observed from this spectrum are due to elements such as gold which was used for coating and elements which are found in the glass substrate. This technique confirmed that there are indeed two layers on this junction as elements that constitute to both MoS_2 and NiPc were detected.

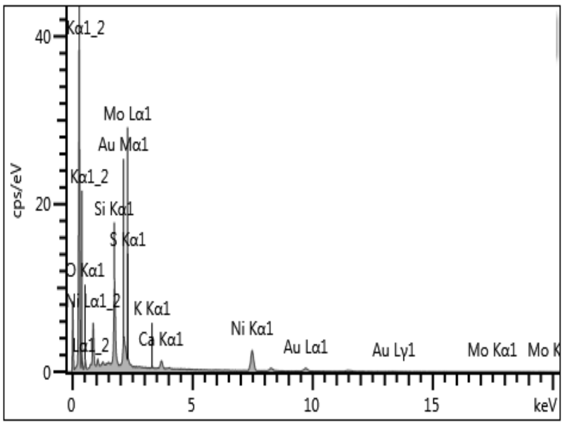

Table 4.1: Table for elemental composition of NiPc/MoS_2 composite.

Element	Wt%	Wt% Sigma	Atomic %
N	25.95	1.20	47.43
O	16.07	0.57	25.71
Al	0.92	0.15	0.87
Si	1.71	0.13	1.56
S	2.97	0.26	2.37
Ca	0.39	0.10	0.25
Ni	46.82	0.94	20.42
Mo	5.18	0.84	1.38
Total:	100.00		100.00

Figure 4.11: EDS spectra of NiPc/MoS_2 composite.

EDS was also used to confirm the elemental composition of all the elements in the layers NiPc/WS_2. Figure 4.12 shows the EDS energy spectrum for NiPc/WS_2 and it confirms the presence of all the elements found in these two materials which are W, N, S and Ni.

© University of Pretoria

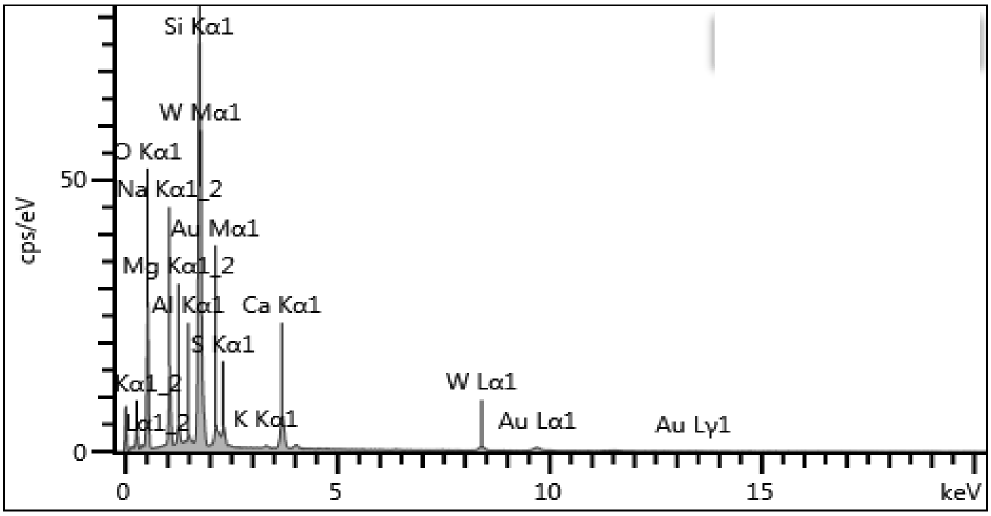

Figure 4.12: EDS spectra for NiPc/WS_2 bilayer.

Similar results were observed for the CuPc/TMD, MnPc/TMD and FePc/TMD composites.

4.4 Characterisation of doped TMDs

4.4.1 XRD

After doping MoS_2 with Au, the thin film sample underwent XRD characterisation. The results of these characterisation are shown in Figure 4.13. It is expected that the peaks of both Au and MoS_2 nanosheets be observed on the XRD spectrum. The unidentified peaks are due to the glass substrate as previously described. The weak intensity peak observed at 15.1° is indexed (002). This peak occurs as a result exfoliation of MoS_2 into 2D nanosheets. The peak observed at 32.5° is indexed (100). It is not clear why this peak is observed but it has been reported previously by Qiao *et al*. (2017) [13]. This peak might be the (100) peak of MoS_2 as it was also reported to be maintained as well after exfoliation [13]. The peaks for Au where indexed using the JCPDS. File no. 89-3697. The peaks observed at 37.8° and 44.5°, indexed (111) and (200), respectively, matched with Au peaks observed from the JCPDS file no. 89-3697 [14]. XRD confirmed that MoS_2 nanosheets were successfully doped with Au.

© University of Pretoria

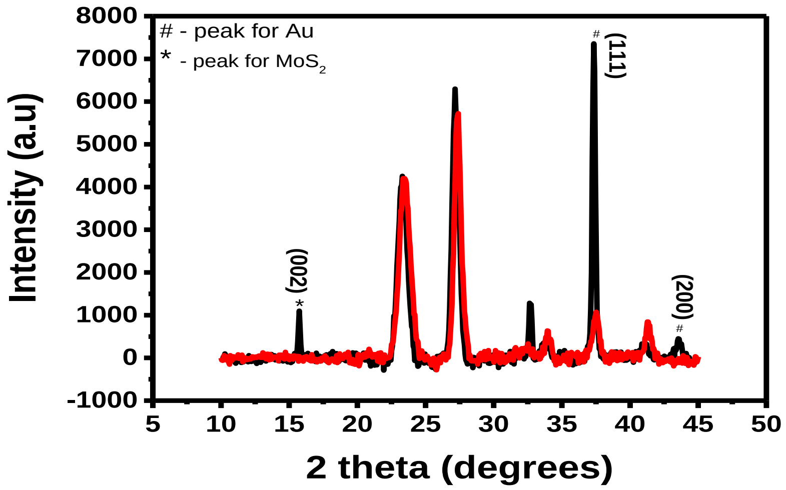

Figure 4.13: XRD spectra for (a) (black) Au-MoS_2 deposited on a glass substrate and b) (red) the substrate.

WS_2 was also subjected to Au doping to yield Au-WS_2. The XRD spectrum, exhibited peaks for both Au and WS_2 (Figure 4.14). The peaks shown on the diffractogram on Figure 4.14 are observed at 14.4°, 28°, 31.8°, 38° and 44°. The peak that is observed at 14.4° is indexed (002) peak. This peak, as discussed for Au-MoS_2, is as a result of the WS_2 2D nanosheets. The next peak is observed at 31.8° and it is indexed (100). As stated for Au-MoS_2, this peak might be resulting due to WS_2 nanosheets. The remaining two peaks are characteristic peaks of Au and they are found at 2 theta (degrees) 38° and 44°. These peaks are indexed (111) and (200), respectively and they were indexed using the JCPDS file no. 89-3697 [15]. XRD shows that doping has taken place but further confirmation was required.

© University of Pretoria

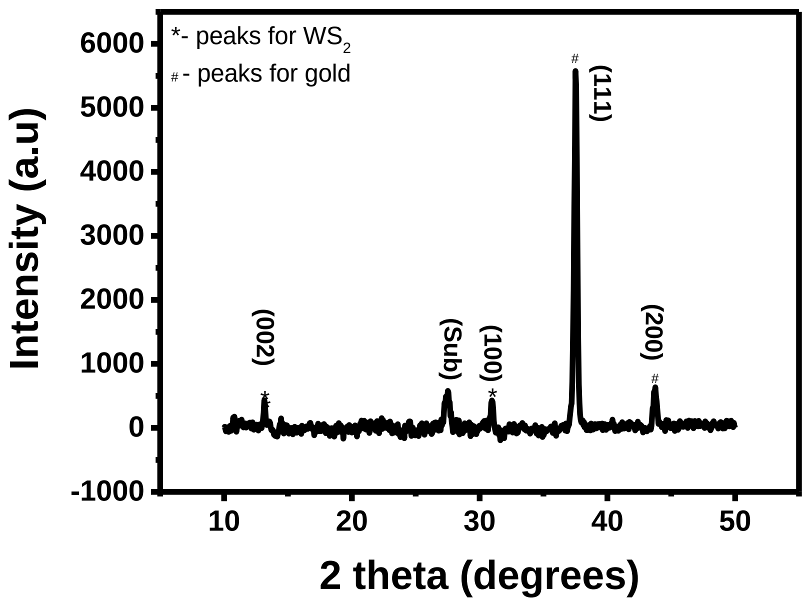

Figure 4.14: XRD spectrum of Au-WS_2

4.4.2 Raman spectroscopy

Raman spectroscopy is a powerful tool for determining if doping has successfully taken place. It can provide information about which type of doping has taken place (n or p-type doping). Generally, n-type doping of TMDs results in softening of the A_{1g} peak resulting in a relative decrease in intensity [16]. This type of doping is also evidenced by a reduction in the distance between E^1_{2g} and A_{1g} [16]. On the other hand, p-type doping generally results in an increase the distance between the two peaks by moving them apart [16]. This p-type doping also results in a Raman spectrum with an increased intensity of the of the A_{1g} peak [16-17]. There are other cases where doping has been successfully executed on TMDs but for such cases, when comparing the Raman spectra for the doped and the pristine TMD, no significant change is observed [18-19].

In this study, Au was used as a dopant on both MoS_2 and WS_2. Previous studies show various findings in terms of Raman spectroscopy. Other studies show that the intensity of the A_{1g} peak increases upon Au-doping on the TMD [16-17]. One study showed that the A_{1g} peak shifts when the TMD is subjected to Au-doping [17].

© University of Pretoria

Figure 4.15 shows the Raman spectrum recorded for Au-MoS_2. Most of the expected results mentioned above were not observed upon applying p-type doping on the TMD using Au. From this spectrum, it is observed that only the E^1_{2g} peak is present. The E^1_{2g} peak observed is found to be blue-shifted at 374 cm^{-1} with respect to the pristine MoS_2. It has been reported previously that Au-S modes are observed between 250 cm^{-1} and 325 cm^{-1} [20]. From the Raman there is a peak that is observed at 320 cm^{-1}. The reason this peak was detected might be because of the Au-S bond in this molecule. Noisy peaks are observed at 380 cm^{-1} ≤ which may suggest some level of crystallinity might have been lost during the doping process. The peaks were observed at relatively low intensities.

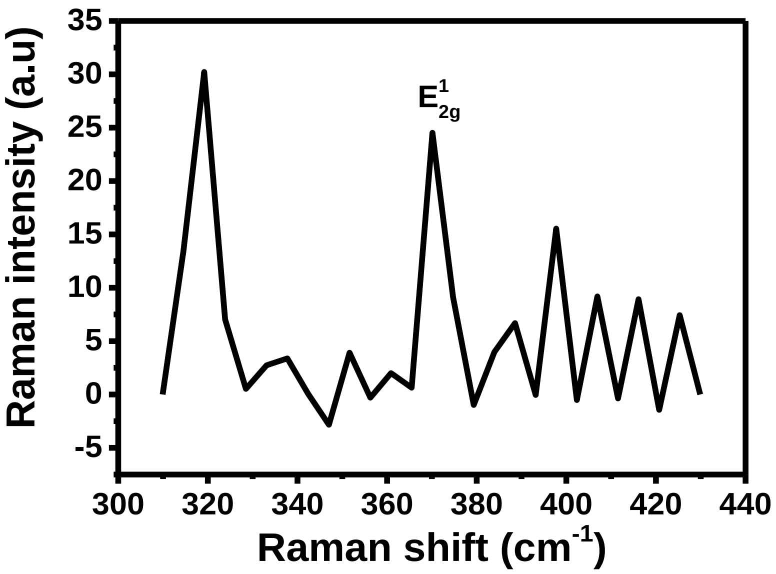

Figure 4.15: Raman spectrum of Au-MoS_2

Figure 4.16 shows the Raman spectrum for Au-WS_2. This spectrum consists of two peaks which are the E^1_{2g} peak and the peak that is in the range of Au-S modes observed at 320 cm^{-1}. Blue shifting of the E^1_{2g} peak is also observed for Au-WS_2 which is a sign of p-type doping. The appearance of the Au-S peak shows that Au is bonded to S which can suggest that Au doping has taken place. The spectrum has noisy peaks as well dominating the spectrum. The peaks were observed at relatively low intensities.

© University of Pretoria

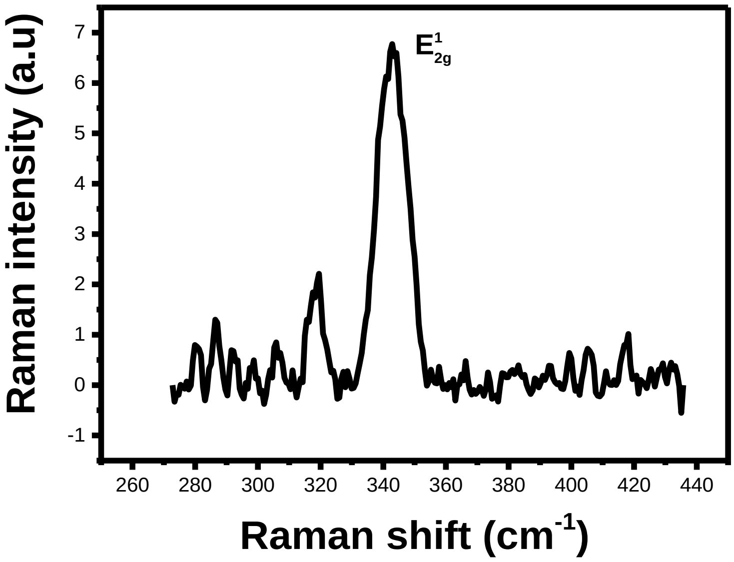

Figure 4.16: The Raman spectrum of Au-WS_2.

4.4.3 EDS

After MoS_2 underwent Au doping, the sample was taken for EDS to see the elements present in the sample. Figure 4.17 shows the EDS spectrum for Au-MoS_2. The presence of Au and elements of the TMD was enough to confirm that doping has occurred. This technique confirmed that all the elements making up Au-MoS_2 are present. These elements are detected at different eV regions of the spectrum. The Au peak occurs at 2.12 eV, the Mo peaks at 2.29 eV and 8.40 eV and lastly, S peak at 2.31 eV. There are other elements that are detected but do not form part of the sample. As explained in section 4.3.1, all these other elements are elements of the glass substrate.

© University of Pretoria

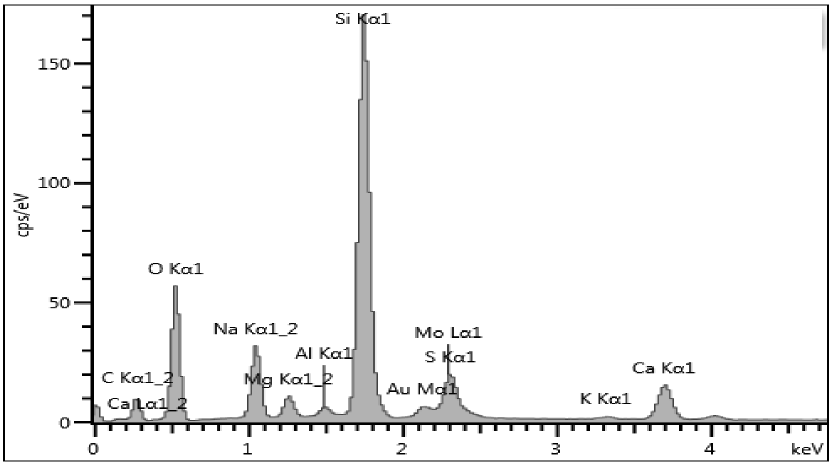

Figure 4.17: EDS spectrum of Au-MoS_2 on a glass substrate.

Au-WS_2 also underwent EDS analysis to confirm if all the elements of the doped material are detected. From this spectrum (Figure 4.18), it is observed that all the elements that are available in the material are detected. This is evidenced by the availability of Au peaks occurring at 2.12 eV and 9.71 eV, W peaks at 1.78 eV and 8.40 eV and S peak at 2.31 eV. Other foreign peaks are observed and they correspond to glass elements.

Together with XRD results, Raman spectroscopy and EDS has proved that doping of WS_2 with Au has taken place.

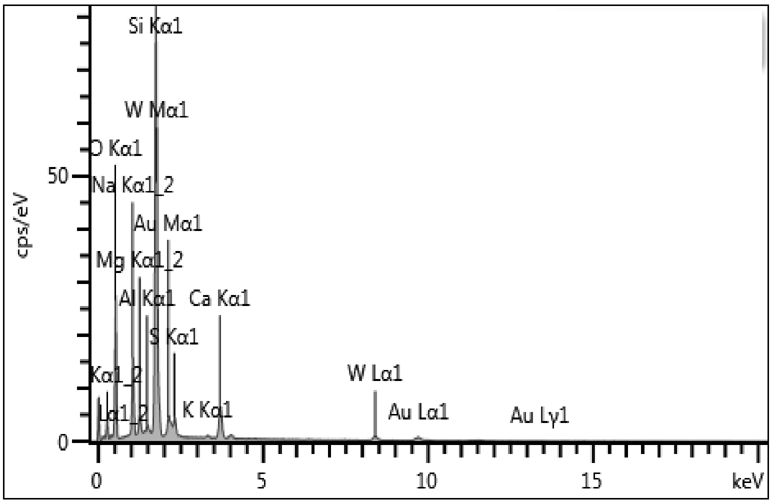

Figure 4.18: EDS spectrum of Au-WS_2.

© University of Pretoria

4.5 Characterisation of solar cell devices

The I-V measurements of devices are a graphical representation of the relationship between the current (I) and voltage (V) of a device. It helps to understand parameters of devices in an electronic circuit. There are many different types of devices which possess different I-V curves with different shapes [21].

The first type of a device is a resistor or an ohmic device. This device obeys ohm's law. This device is the simplest device and has an I-V curve which is linear and intercepts the origin. These types of devices are considered to be passive as they don't generate electricity [21-22].

The second type of device is a diode. Diodes are p-n junction devices. In comparison to ohmic devices, diodes have a nonlinear relationship between current and voltage suggesting that they do not obey ohm's law. The device has an I-V curve that increases exponentially at positive voltages meaning that current moves freely in the device. The importance of a diode is rectification which is the conversion of alternating current (AC) to direct current (DC). Rectification occurs if you apply potential to the anode of the diode and the current pass (forward-biased current) and when potential is applied to the cathode, current is blocked (reverse-biased current). The diode needs to be biased for current to flow [21, 23].

The third type of a device is a solar cell device. This type of device behaves like a diode under dark I-V measurements. The measurements taken under dark conditions for a solar cell can be used to check if the device shows rectification. Under illuminated conditions, solar cells have the same curve that it is exhibited for dark I-V measurements but shifted downwards as a result of response to light. This new curve will be able to give information about parameters such as fill factor, short circuit current, open circuit voltage and the power output of the device. All these parameters can then be used to calculate the percentage coefficient efficiency of the solar cell [21, 24].

Various devices have been fabricated for this study and underwent I-V measurements to see if they respond as solar cells.

© University of Pretoria

4.5.1 Dark and illuminated I-V measurements of fabricated solar cell devices

4.5.1.1 Dark and illuminated I-V measurements of the Glass/FTO/Au-MoS_2/CuPc/MoS_2/Au device

Figure 4.19 shows the I-V characterisation results for the device with the architecture Glass/FTO/Au-MoS_2/CuPc/MoS_2/Au. Figure 4.19a shows the current against voltage curve of the device under (1) dark and (2) illuminated conditions. Figure 4.19b shows a semi-log curve of current against voltage curve of the device under (1) dark and (2) illuminated conditions.

Considering Figure 4.19a, curve 1 shows that under dark conditions, when voltage is 1 V, the recorded current is 0.01 A. The shape this curve exhibits is quadratic [25] implying that a quadratic relationship between current and voltage is observed which is almost linear and this type of dependence has been reported before. This implies that the device is not purely ohmic and there is a slight rectification exhibited by the device. The fact that this curve is slightly rectifying is confirmed by the first curve (1) on Figure 4.19b which is a semi-log curve of current and voltage of the device under dark conditions. The curve is asymmetric as it shows that the forward-biased and the reverse-biased current are not the same. The forward-biased current is slightly higher than the reverse-biased current. This shows that there is rectification in the device. However, the difference between the current values for forward-biased and reverse-biased is small suggesting that there is a little rectification observed from the device.

Shifting the focus to I-V characterisation of the device under illuminated conditions, Figure 4.19a curve 2 is a plot of current against voltage under these illuminated conditions. This curve shows that at voltage of 1 V, the current is ~0.015 A. This implies that more current is generated under illuminated I-V measurements than in dark I-V measurements. This is also viewed for the semi-log plot of current against voltage of the device under illuminated conditions. (Figure 4.19b curve 2). A conclusion drawn from this is that the device is sensitive and can absorb visible light. The active layer of this device, CuPc, has been shown by UV-vis studies that it has a high sensitivity to the visible region of the electromagnetic spectrum. As such, this material is a good photon absorber and suitable for being used as the photoactive layer in solar cells.

© University of Pretoria

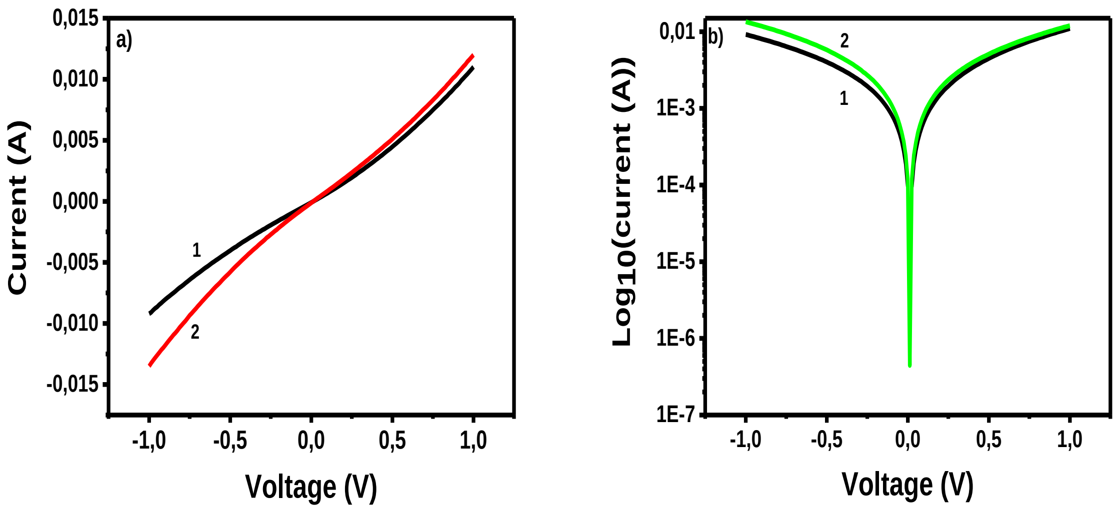

Figure 4.19 a) I-V measurements of Glass/FTO/Au-MoS_2/CuPc/MoS_2/Au device under 1) dark conditions and 2) illuminated conditions. Figure 4.19 b) voltage against $\log_{10}$(Current) for Glass/FTO/Au-MoS_2/CuPc/MoS_2/Au device measured in (1) dark and (2) illuminated conditions.

4.5.1.2 Dark and illuminated I-V measurements of the Glass/FTO/Au-WS_2/CuPc/WS_2/Au device.

The Glass/FTO/Au-WS_2/CuPc/WS_2/Au device was also fabricated and it underwent both dark and illuminated I-V characterisations. Figure 4.20a shows the current against voltage curve of the device under both dark and illuminated conditions. Curve 1 shows the dark measurements of the device while curve 2 shows measurements taken under illuminated conditions. Converting the measured results into semi-log plot of current and voltage, Figure 4.20b shows the semi-log plot of current and voltage under both dark and illuminated conditions with the curves labelled 1 and 2, respectively.

From Figure 4.20a, curve 1 (dark I-V measurements) shows quadratic curve which is slightly linear. The current observed when voltage is 2 V for dark I-V measurements is 0.032 A. The semi-log plot for current against voltage of the device under dark measurements also confirms that a slight rectification exists for the device. Figure 4.20b curve 1 shows that the reverse-biased current is having slightly different values as compared to the forward-biased current. However, the difference between the

© University of Pretoria

reverse-biased and forward-biased current is small which shows that this device is slightly rectifying.

For illuminated conditions, figure 4.20a curve 2 shows the current against voltage plot of the device under these conditions. Illuminated conditions shows that current measured at -2 V is 0.043. This implies that more current is generated under illuminated conditions as compared to dark conditions implying that the device is sensitive to visible light. The semi-log plot curve under illuminated conditions is also above the curve for dark conditions further proving that the device is sensitive to visible light.

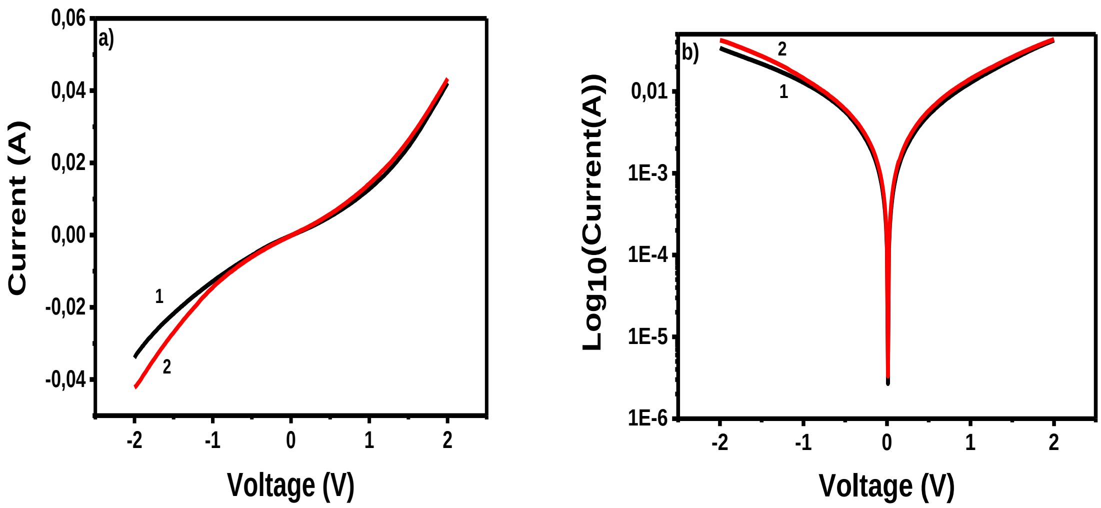

Figure 4.20 a) I-V measurements of Glass/FTO/Au-WS_2/CuPc/WS_2/Au device under 1) dark conditions and 2) illuminated conditions. Figure 4.20 b) voltage against log_{10}(Current) for Glass/FTO/Au-WS_2/CuPc/WS_2/Au device measured in a) dark and b) illuminated conditions.

4.5.1.3 Dark and illuminated I-V measurements of the Glass/FTO/Au-MoS_2/FePc/MoS_2/Au device

The device with the architecture Glass/FTO/Au-MoS_2/FePc/MoS_2/Au was fabricated and underwent both dark and illuminated I-V measurements. Figure 4.21a shows voltage against current curve of the device with curve 1 demonstrating the measurements taken under dark conditions and curve 2 demonstrating measurements taken under illuminated conditions. Figure 4.21b shows the semi-log curve of current against voltage of the device with curve 1 representing measurements taken under

© University of Pretoria

dark conditions and curve 2 demonstrating measurements taken under illuminated conditions.

Figure 4.21a curve 1 shows the curve of current against voltage under dark conditions. As reported for CuPc based devices, the curve observed for this measurement is a quadratic curve which is slightly linear. Checking the semi-log curve of current against voltage, Figure 4.21b curve 1, which is a measurement taken under dark characterisations, the reverse-biased and the forward-biased current are slightly different. The forward-biased current is slightly above the reverse-biased current proving that there is a slight rectification exhibited by the device. The device shows a current of 0.039 A at voltage of 2 V for dark measurements.

Figure 4.21a curve 2 shows current against voltage curve for illuminated conditions. The curve also shows a quadratic shape. The current measured between -2 V and -1 V is found to be higher compared to the current recorded for dark measurements. This is also observed for the semi-log curve for current and voltage.

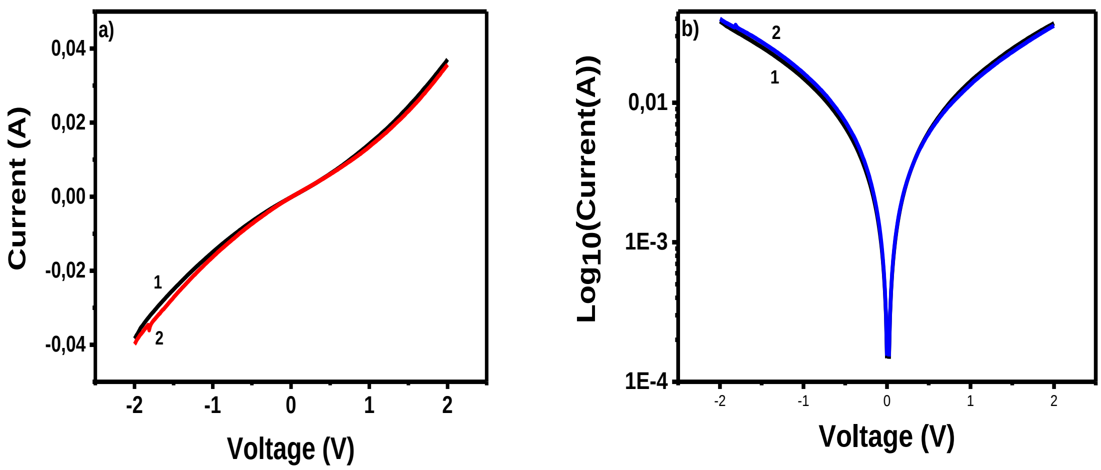

Figure 4.21 a) I-V measurements of Glass/FTO/Au-MoS_2/FePc/MoS_2/Au device under 1) dark conditions and 2) illuminated conditions. Figure 4.21 b) voltage against log_{10}(Current) for Glass/FTO/Au-MoS_2/FePc/MoS_2/Au device measured in 1) dark and 2) illuminated conditions.

© University of Pretoria

4.5.1.4 Dark and illuminated I-V measurements of the Glass/FTO/Au-WS_2/FePc/WS_2/Au device

The device with the architecture Glass/FTO/Au-WS_2/FePc/WS_2/Au was fabricated and taken for dark and illuminated I-V characterisations. Figure 4.22a shows the curve of current against voltage with curve 1 being the measurements taken under dark conditions and curve 2 being measurements taken under illuminated conditions. Figure 4.22b shows the semi-log curves for current against voltage measurements. curve 1 shows the measurements taken under dark conditions while curve 2 shows the measurements taken under illuminated conditions.

Figure 4.22a curve 1 shows characterisation of devices under dark conditions. This curve demonstrates the current against voltage relationship of the device under dark conditions. The shape of the curve observed is quadratic which is slightly linear. The maximum current observed for this device is 0.015 A. Considering the semi-log curve of current against voltage, Figure 4.22b curve 1 shows that the curve is slightly asymmetric meaning that the reverse-biased current is slightly lower than the forward-biased current. This proves that there is a slight rectification but it is not enough to make the device act as a solar cell.

Figure 4.22a curve 2 shows the current against voltage measurements taken under illuminated conditions. The curve has a quadratic shape which as well is slightly linear. The curve has its maximum current being 0.0175 A which is greater than the maximum current for dark measurements. Most sections of the curve are not overlapping with those of dark characterisation curve. This shows that the device is sensitive to visible light.

© University of Pretoria

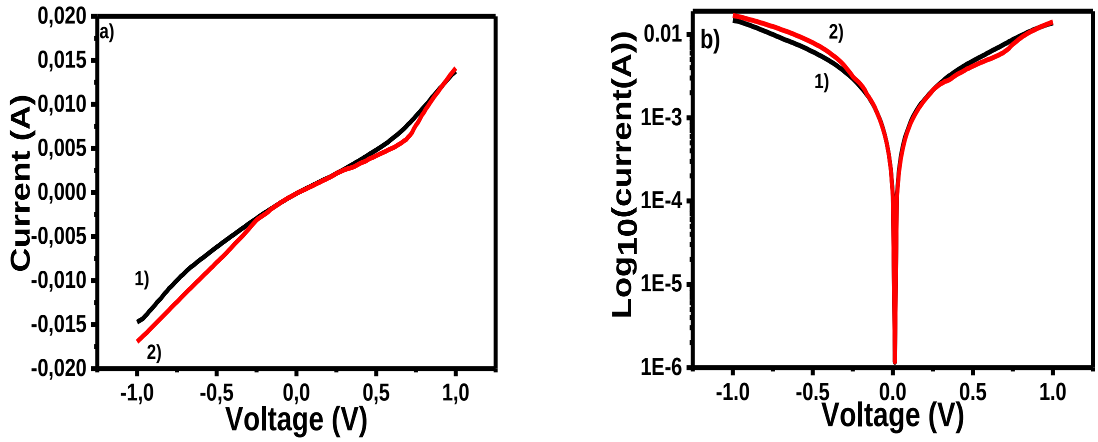

Figure 4.22 a) I-V measurements of Glass/FTO/Au-WS_2/FePc/WS_2/Au device under 1) dark conditions and 2) illuminated conditions. Figure 4.22 b) voltage against log_{10}(Current) for Glass/FTO/Au-WS_2/FePc/WS_2/Au device measured in 1) dark and 2) illuminated conditions.

4.5.1.5 Dark and illuminated I-V measurements for the Glass/FTO/Au-MoS_2/MnPc/MoS_2/Au device

The device with the architecture of Glass/FTO/Au-MoS_2/MnPc/MoS_2/Au underwent dark and illuminated I-V measurements. Figure 4.23a shows the current against voltage curves with curve 1 being the current against voltage measurements taken in dark conditions while curve 2 represents the measurements taken in illuminated conditions. Figure 4.23b shows the semi-log curve for current against voltage measurements with curve 1 being measurements taken under dark conditions while curve 2 representing measurements taken under illuminated conditions.

Figure 4.23a shows the current against voltage measurements for the device with curve 1 showing those measurements taken under dark conditions. The curve is quadratic and near-linear as well which suggest the device is not purely ohmic and is not entirely passive. This implies that there is a slight rectification exhibited by the device. The maximum current observed by the device is 0.058 A. Figure 4.23b curve 1 shows the semi-log curve for current against voltage of the device under dark conditions. This curve is not completely symmetric as the forward and the reverse-

© University of Pretoria

biased currents differ by a small margin, further implying that the device is slightly rectifying.

Figure 4.23a curve 2 shows the current against voltage curve of the device under illuminated conditions. The curve's shape is quadratic as well and it is not overlapping with a curve 1. The maximum current observed for this curve is 0.062 A which is higher than the maximum current reported for dark characterisation. Figure 4.23b curve 2 is not completely aligned with curve 1. All these suggests that the device is sensitive to visible light and this has been proven by UV-vis measurements which showed the photoactive layer in this device, MnPc, to have an intense absorption in the visible region of the electromagnetic spectrum.

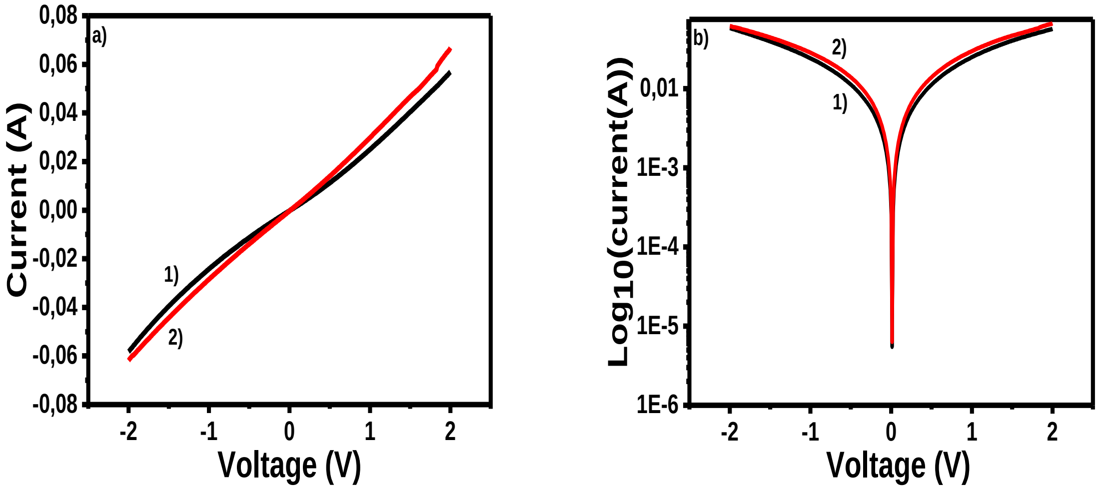

Figure 4.23 a) I-V measurements of Glass/FTO/Au-MoS_2/MnPc/MoS_2/Au device under 1) dark conditions and 2) illuminated conditions. Figure 4.23 b) voltage against $\log_{10}$(Current) for Glass/FTO/Au-MoS_2/MnPc/MoS_2/Au device measured in 1) dark and 2) illuminated conditions.

4.5.1.6 Dark and illuminated I-V measurements for the Glass/FTO/Au-WS_2/MnPc/WS_2/Au device

The device with the architecture Glass/FTO/Au-WS_2/MnPc/WS_2/Au underwent dark and illuminated I-V measurements. Figure 4.24a shows the current against voltage curves with curve 1 indicating measurements taken under dark conditions and curve 2 showing measurements taken under illuminated conditions. Figure 4.24b shows the

© University of Pretoria

semi-log curves for current against voltage measurements with curve 1 indicating measurements taken under dark conditions while curve 2 shows measurements taken under illuminated conditions.

Figure 4.24a shows current against voltage curve with curve 1 showing measurements taken under dark conditions. The shape displayed by this curve is a quadratic shape and it is slightly linear which shows that the device is not purely ohmic or resisting. This implies that there is a slight rectification exhibited by the device. The maximum current of this curve is slightly below that of curve 2 and has a value of 0.042 A. Figure 4.24b shows the semi-log curve for current against voltage with curve 1 showing the dark measurements. This curve shows a very small difference between the reverse-biased and forward-biased current. This implies that the curve has a very small rectification.

Figure 4.24a curve 2 shows current against voltage curve taken under illuminated conditions. This curve has a maximum voltage of 0.044 A. This is slightly above the voltage for curve 1. Figure 4.24b curve 2 shows the semi-log curve current against voltage under illuminated condition. The curve is above curve 2 by a small margin but shows that the device is sensitive to light.

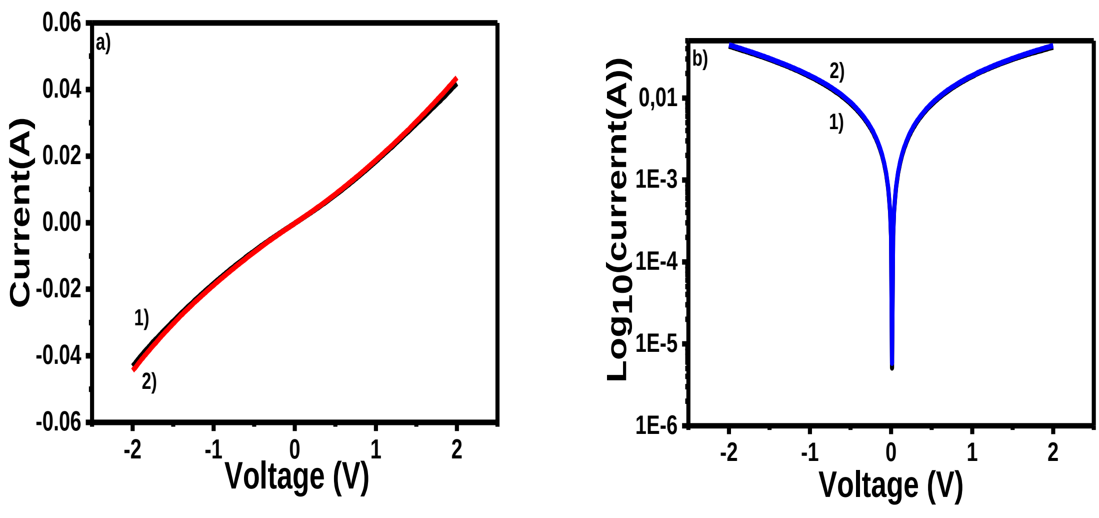

Figure 4.24 a) I-V measurements of Glass/FTO/Au-WS_2/MnPc/WS_2/Au device under 1) dark conditions and 2) illuminated conditions. Figure 4.24 b) voltage against $\log_{10}$(Current) for Glass/FTO/Au-WS_2/MnPc/WS_2/Au device measured in 1) dark and 2) illuminated conditions

© University of Pretoria

4.5.1.7 Dark and illuminated I-V measurements for the Glass/FTO/Au-MoS_2/NiPc/MoS_2/Au device

The device with the architecture Glass/FTO/Au-MoS_2/NiPc/MoS_2/Au underwent dark and illuminated I-V measurements. Figure 4.25a shows the current against voltage curves with curve 1 indicating measurements taken under dark conditions and curve 2 showing measurements taken under illuminated conditions. Figure 4.25b shows the semi-log curves for current against voltage measurements with curve 1 indicating measurements taken under dark conditions while curve 2 shows measurements taken under illuminated conditions.

Figure 4.25a shows the current against voltage measurements for the device with curve 1 showing those measurements taken under dark conditions. The curve is quadratic and near-linear as well which suggest the device is not purely ohmic and is not entirely passive. This implies that there is a slight rectification exhibited by the device. The maximum current observed by the device is 0.015 A. Figure 4.25b curve 1 shows the semi-log curve for current against voltage of the device under dark conditions. This curve is not completely symmetric as the forward and the reverse-biased currents differ by a small margin, further implying that the device is slightly rectifying.

For illuminated conditions, figure 4.25a curve 2 shows the current against voltage plot of the device under these conditions. Illuminated conditions shows that the maximum current is 0.0175. This implies that more current is generated under illuminated conditions as compared to dark conditions implying that the device is sensitive to visible light. The semi-log plot curve under illuminated conditions is also above the curve for dark conditions further proving that the device is sensitive to visible light.

© University of Pretoria

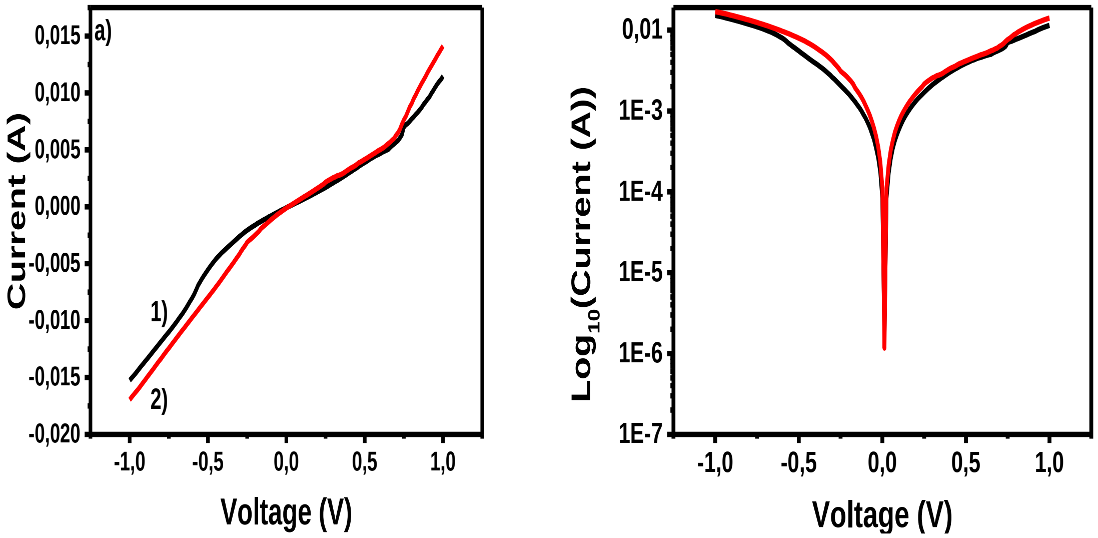

Figure 4.25 a) I-V measurements of Glass/FTO/Au-MoS_2/NiPc/MoS_2/Au device under 1) dark conditions and 2) illuminated conditions. Figure 4.25 b) voltage against log_{10}(Current) for Glass/FTO/Au-MoS_2/NiPc/MoS_2/Au device measured in 1) dark and 2) illuminated conditions

4.5.1.8 Dark and illuminated I-V measurements for the Glass/FTO/Au-WS_2/NiPc/WS_2/Au device

The device with the architecture Glass/FTO/Au-WS_2/NiPc/WS_2/Au underwent dark and illuminated I-V measurements. Figure 4.26a shows the current against voltage curves with curve 1 indicating measurements taken under dark conditions and curve 2 showing measurements taken under illuminated conditions. Figure 4.26b shows the semi-log curves for current against voltage measurements with curve 1 indicating measurements taken under dark conditions while curve 2 shows measurements taken under illuminated conditions.

Figure 4.26a shows current against voltage curve with curve 1 showing measurements taken under dark conditions. The shape displayed by this curve is a quadratic shape and it is slightly linear which shows that the device is not purely ohmic or resisting. This implies that there is a slight rectification exhibited by the device. The maximum current of this curve is slightly below that of curve 2 and has a value of 0.039 A. Figure 4.26b shows the semi-log curve for current against voltage with curve 1 showing the

© University of Pretoria

dark measurements. This curve shows a very small difference between the reverse-biased and forward-biased current. This implies that the curve has a very small rectification.

Figure 4.26a curve 2 shows current against voltage curve taken under illuminated conditions. This curve has a maximum voltage of 0.048 A. This is slightly above the voltage for curve 1. Figure 4.26b curve 2 shows the semi-log curve current against voltage under illuminated condition. The curve is above curve 2 by a small margin but shows that the device is sensitive to light.

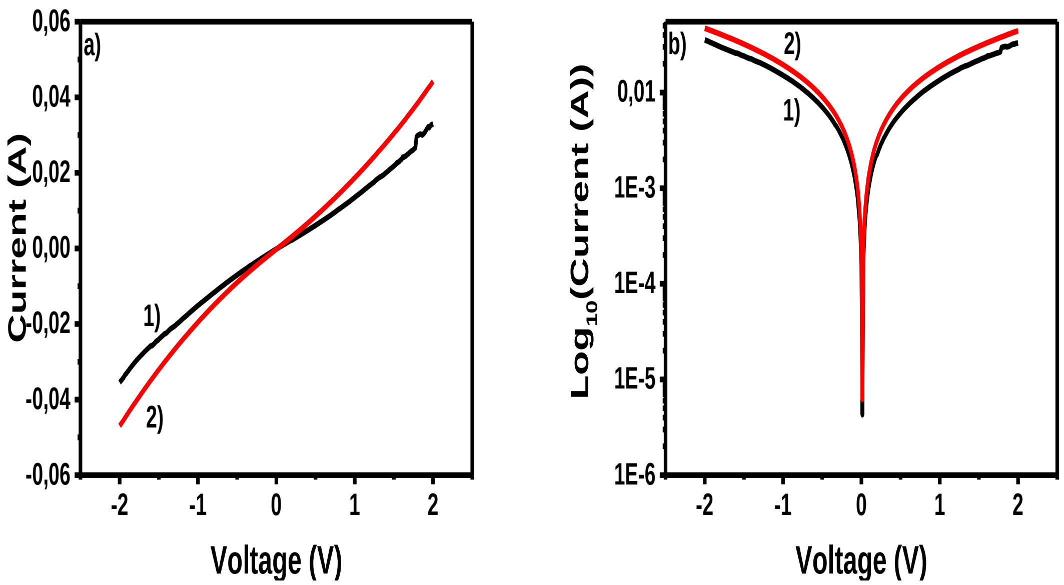

Figure 4.26 a) I-V measurements of Glass/FTO/Au-WS_2/NiPc/WS_2/Au device under 1) dark conditions and 2) illuminated conditions. Figure 4.26 b) voltage against log_{10}(Current) for Glass/FTO/Au-WS_2/NiPc/WS_2/Au device measured in 1) dark and 2) illuminated conditions.

Table 4.2 highlights the comparison of maximum current recorded for each device under dark and illuminated conditions. A general observation from this comparison is that for all the devices, the maximum current recorded under dark conditions is higher than the maximum current under illuminated conditions. This shows that all the devices are absorbing light and generating current consequently. From Table 4.2, it can be

© University of Pretoria

deduced that the solar cell that gave the best performance in terms of absorption of light is the device with the architecture Glass/FTO/Au-WS_2/CuPc/WS_2/Au. This solar cell device, together with the Glass/FTO/Au-MoS_2/CuPc/MoS_2/Au device showed the best performance in terms of rectification as they had an observable but yet small difference between the forward-biased current and the reverse-biased current.

Table 4.2 shows the I-V responses of the fabricated solar cells.

	Dark		Illuminated	
Solar cell	V_{max} (V)	I_{max} (A)	V_{max} (V)	I_{max} (A)
Glass/FTO/Au-MoS_2/CuPc/MoS_2/Au	1	0.010	1	0.015
Glass/FTO/Au-WS_2/CuPc/WS_2/Au	2	0.032	2	0.043
Glass/FTO/Au-MoS_2/FePc/MoS_2/Au	2	0.039	2	0.041
Glass/FTO/Au-WS_2/FePc/WS_2/Au	1	0.015	1	0.0175
Glass/FTO/Au-MoS_2/MnPc/MoS_2/Au	2	0.058	2	0.062
Glass/FTO/Au-WS_2/MnPc/WS_2/Au	2	0.042	2	0.044
Glass/FTO/Au-MoS_2/NiPc/MoS_2/Au	1	0.015	1	0.0175
Glass/FTO/Au-WS_2/NiPc/WS_2/Au	2	0.048	2	0.039

In conclusion, all the devices fabricated in this study show a very small rectification as demonstrated by both their dark and illuminated I-V measurements. The fact that these devices have a small amount of rectification indicates that they have unfavourable performance for them to be considered for solar cells application. However, since all these devices are not completely ohmic and they show a quadratic relationship between current and voltage, it shows that improvements can be implemented on these devices and tweaks can be made in order to boost their performances.

The low solar cell performance of the devices might be because the MPc's used as photoactive layers are weakly p-type. This implies that the charge carriers that are dominating are holes. One other property known for MPc is that they have a relatively low charge carrier mobility [26]. Having the holes dominating the sample and a low carrier mobility, a device may experience more electron-hole recombination leading to

© University of Pretoria

unfavourable performances. This problem can be solved by fabrication of a bulk heterojunction system as an active layer. This bulk heterojunction system should be consisting of MPc's as the acceptor materials since they are p-type and other n-type organic materials such as fullerenes as donors. Most solar cells that employ MPc's as their photoactive layer have these material as part of a bulk heterojunction over these MPc's being used alone [27-28].

© University of Pretoria

4.6 References

[1] V. Štengl,J. Henych, M. Slušná and P. Ecorchard, "Ultrasound exfoliation of inorganic analogues of curveene," *Nanoscale Res. Lett.,* vol. 9, pp 167-181, 2014.

[2] H. Ma, Z. Shen, and S. Ben, "Understanding the exfoliation and dispersion of MoS_2 nanosheets in pure water," *J. Colloid Interface Sci.*, vol. 517, pp. 204–212, 2018.

[3] M. Park, T. P. Nguyen, K. S. Choi, and J. Park, "MoS_2-nanosheet / curveene-oxide composite hole injection layer in organic light-emitting diodes MoS_2 -Nanosheet / Curveene-Oxide Composite Hole Injection Layer in Organic Light-Emitting Diodes," *Electron. Mater. Lett.*, vol. 13, pp. 344-350, No. 4, 2017.

[4] R. Jha and P. K. Guha, "An effective liquid-phase exfoliation approach to fabricate tungsten disulfide into ultrathin two- dimensional semiconducting nanosheets," *J. Mater. Sci.*, vol. 52, pp. 7256–7268, 2017.

[5] V. Kaushik, S. Wu, H. Jang, J. Kang, and K. Kim, "Scalable exfoliation of bulk MoS_2 to single- and few-layers using toroidal taylor vortices," *nanomaterials,* vol. 8, pp 587-598, 2018.

[6] F. Wang, I. Kinloch, D. Wolverson, and R. Tenne, "Strain-induced phonon shifts in tungsten disulfide nanoplatelets and nanotubes," *2D Mater*., vol. 4, pp. 2-12, no. 015007, 2016.

[7] H. Zeng, G. Liu, J. Dai, and S. J. Xu, "Optical signature of symmetry variations and spin-valley coupling in atomically thin tungsten dichalcogenides," *Scientific Reports.* vol. 3, pp. 1-5, no. 1608, 2013.

[8] H. K. Adigilli, B. Padya, L. Venkatesh, V. S. K. Chakravadhanula, A. K. Pandey, and J. Joardar, "Oxidation of 2D-WS_2 nanosheets for generation of 2D-WS_2/WO_3 heterostructure and 2D and nanospherical WO_3," *Phys. Chem. Chem. Phys*., vol. 21, pp. 25139–25147, 2019.

[9] S. Kumar, N. Kaur, K. Sharma, and A. Mahajan, " Improved Cl_2 sensing characteristics of reduced curveene oxide when decorated with copper phthalocyanine nano flowers," *RSC Adv.*, vol. 7, pp. 25229–25236, 2017.

© University of Pretoria

[10] T. Zou, X. Wang, H. Ju, L. Zhao, T. Guo, W. Wu and H. Wang, “Controllable molecular packing motif and overlap type in organic nanomaterials for advanced optical properties," *Crystals*, vol. 8, no. 22, pp. 1-12, 2018.

[11] Z. Xu, G. Zhang, Z. Cao, J. Zhao, and H. Li, “Effect of N atoms in the backbone of metal phthalocyanine derivatives on their catalytic activity to lithium battery Journal of Molecular Catalysis A : Chemical Effect of N atoms in the backbone of metal phthalocyanine derivatives on their catalytic activity to lithium battery,” *J. Mol. Catal. A-Chem.,* vol. 318, pp. 101–105, 2010.

[12] E. Güzel, A. Koca, A. Gül, M. B. Koçak “Microwave-assisted synthesis , electrochemistry and spectroelectrochemistry of amphiphilic phthalocyanines,” *Synthetic Metals*., vol. 199, pp. 372–380, 2015.

[13] Wayne D. Niemeyer, “SEM/EDS analysis for problem solving in the food industry “, *Proc. SPIE 9636*, Scanning Microscopies, 2015.

[14] X. Qiao, Z. Zhang, and F. Tian, “Enhanced catalytic reduction of p-nitrophenol on ultrathin MoS_2 nanosheets decorated noble-metal nanoparticles Enhanced catalytic reduction of p-nitrophenol on ultrathin MoS_2 nanosheets decorated noble-metal nanoparticles,” *ACS Publications*, vol. 6, pp. 3538-3547, 2017.

[15] J. Shakya, A. S. Patel, F. Singh, and T. Mohanty, “Composition dependent Fermi level shifting of Au decorated MoS_2 nanosheets,” *Appl. Phys. Lett.*, vol. 108, pp. 1-4, no. 013103, 2016.

[16] Y. Shi, J. Huang, L. Jin, Y. Hsu, S. F. Yu, L. Li, and H. Y. Yang., "Selective decoration of Au nanoparticles on monolayer MoS_2 single crystals.", *Scientific reports,* vol. 3, no. 1839, 2013.

[17] S. S. Singha, D. Nandi and A. Singha., "Tuning the photoluminescence and ultrasensitive trace detection properties of few-layer MoS_2 by decoration with gold nanoparticles", *RSC Adv,* Vol. 5, pp. 24188–24193, 2015.

[18] M. R. Laskar, D. N. Nath, L. Ma, E. W. Lee, C. H. Lee, T. Kent, Z. Yang, R. Mishra, M. A. Roldan, J. Idrobo, S. T. Pantelides, S. J. Pennycook, R. C. Myers, Y. Wu and S. Rajan., "p-type doping of MoS_2 thin films using Nb", *Appl. Phys. Lett.*, vol. 104, no. 092104, 2014.

© University of Pretoria

[19] M. Chuang, S. Yang and F. Chen., " Metal nanoparticle-decorated two-dimensional molybdenum sulfide for plasmonic-enhanced polymer photovoltaic devices", *Materials*, vol. 8, pp 5414-5425, 2015.

[20] V. Birte, O. Patric, L. Sandra, K. Chanaka, D. Amala and B. Thomas., "Structural information on the Au-S Interface of thiolate-protected goldclusters: A Raman spectroscopy study", *J. Phys. Chem.,* vol. 18, pp 9604-9611, 2014.

[21] Electronictutorials, "I-V characteristics curves", *electronictutorials*, January 21, 2020, https://www.electronics-tutorials.ws/blog/i-v-characteristic-curves.html

[22] Boundless physics, "Resistance and resistors" *lumen candela*, January 21, 2020, https://courses.lumenlearning.com/boundless-physics/chapter/resistance-and-resistors/

[23] C. Rossi, P. Buccella, C. Stefanucci, J. Sallese., " SPICE modeling of photoelectric effects in silicon with generalized devices", *IEEE J. Electron Devi.*, vol. 6, pp 987-995, 2018.

[24] M. Neukom, S. Züfle, S. Jenatsch and B. Ruhstaller., "Opto-electronic characterization of third generation solar cells Supplemental information", *Fluxim,* January 20, 2020, https://www.fluxim.com/measurement-techniques

[25] J. N. Fru, N. Nombona, and M. Diale, “Physica B : Physics of Condensed Matter Synthesis and characterisation of methylammonium lead tri-bromide perovskites thin films by sequential physical vapor deposition,” *Phys. B Phys. Condens. Matter*, vol. 578, pp. 1-10, no. 411884, 2020.

[26] H. Yamada and N. Ono, “Organic semiconductors based on small molecules with thermally or photochemically removable groups,” *Chem. Commun*, pp. 2957–2974, 2008.

[27] R. B. Pode, “On the problem of open circuit voltage in metal phthalocyanine / C_{60} organic solar cells,” *Adv. Mat. Lett.*, vol. 2, pp. 3-11, 2011.

[28] A.B. Djuriši, C.Y. Kwong, P.C. Chui and W.K. Chan, “Indium–tin–oxide surface treatments: Influence on the performance of CuPc/C_{60} solar cells,” *J. Appl. Phys.*, vol. 93, no. 9, pp. 5472-5479, 2003.

© University of Pretoria

© University of Pretoria

Chapter 5: Conclusions and recommendations

5.1 Conclusions

Mono to few layered TMDs (WS_2 and MoS_2) were successfully synthesised through a liquid-assisted exfoliation method from their bulk counterparts. To achieve this step, sonication time as well as the solvent to be used for exfoliation were carefully put into consideration. Successful synthesis of TMDs was confirmed by several characterisation techniques such as XRD, Raman spectroscopy and SEM. The TMD nanosheets underwent p-type doping using gold *via* a wet chemical approach. The process was successfully conducted and the resulting materials were Au-MoS_2 and Au-WS_2. Successful doping of these TMD nanosheets was confirmed using XRD and EDS.

Solar cell devices were successfully fabricated in this study. The devices fabricated utilised Au-doped TMDs and pristine TMDs as hole transporting layers (HTL) and electron transporting layers (ETL), respectively. For photoactive layers, these devices used different MPc's (CuPc, FePc, NiPc and MnPc). The resulting devices were tested for solar cell properties and performance using dark and illuminated I-V characterisation.

Dark I-V measurements were used to assess if the devices are rectifying or not. If the devices are found to be rectifying, it means they can be utilised as solar cells. On the other hand, if they do not show any form of rectification, the devices will not be utilised for solar cell applications. When all the devices fabricated in this study underwent dark I-V measurements, they all showed a small amount of rectification. A conclusion drawn from this is that there was rectification but it was too small for the devices to be used for solar cell applications. However, the devices were not completely passive as the relationship between current and voltage was not ohmic (linear) but quadratic instead.

From illuminated I-V characterisation, all the devices had their measurements (curves) not aligned with the curves for measurements taken under dark conditions. The maximum current values recorded for all the devices under illuminated conditions were higher than the maximum current values recorded for under dark measurements. As such, the conclusion drawn is that the devices were found to be sensitive to visible light from sun hence the photoactive materials used in this device are adequate photon absorbers.

© University of Pretoria

5.2 Recommendations

There are gaps which can be identified in this study which implies that this research project can still be taken further. As illustrated in chapter 4, the devices fabricated did not show enough rectification for consideration in solar cell applications.

The following major recommendation is suggested.

It is recommended that instead of using MPc's alone as photoactive layers, a bulk heterojunction system be employed. Examples of mostly utilised bulk heterojunction systems are P3HT:PCBM and MPc:C_{60}. The utilisation of these materials has been shown to improve solar cell performance. The bulk heterojunction recommended should consist of MPc's since they are weakly p-type and another n-type photon absorbing material such as fullerenes.

© University of Pretoria

Appendix

Appendix A: UV-vis curves for various metallophthalocyanines

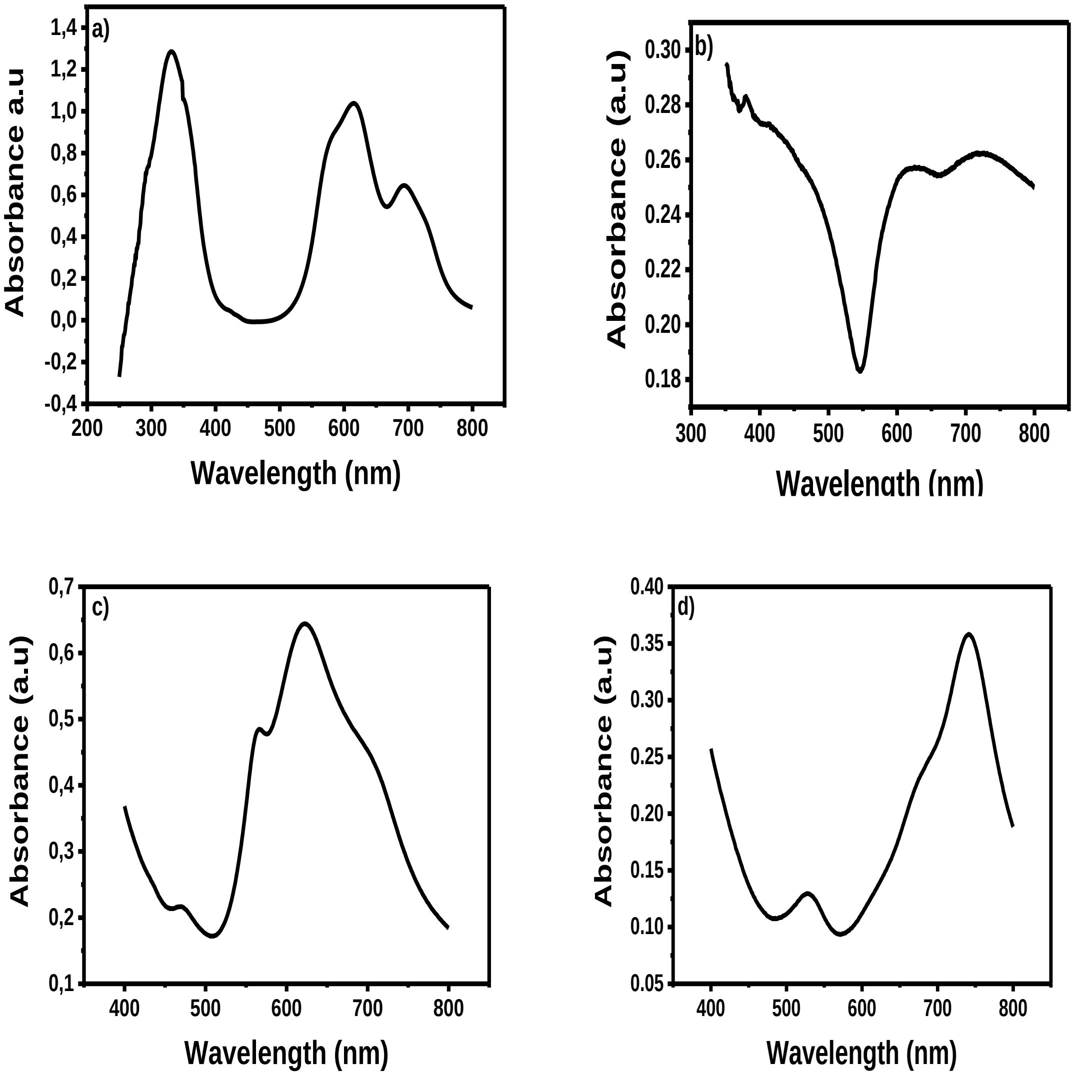

These figures display the UV-vis spectra for (a) CuPc, (b) NiPc, (c) FePc and (d) MnPc.

© University of Pretoria